

Photodissociation dynamics in the first absorption band of pyrrole: II. Photofragment distributions for the

${}^1A_2(\pi\sigma^*) \leftarrow \tilde{X}{}^1A_1(\pi\pi)$ transition

David Picconi* and Sergy Yu. Grebenshchikov†

Department of Chemistry, Technical University of Munich,

Lichtenbergstr. 4, 85747 Garching, Germany

The analysis of the total kinetic energy release (TKER) of the photofragments pyrrolyl + H-atom formed in the photodissociation of pyrrole in the low-lying state ${}^1A_2(\pi\sigma^*)$ is presented. The TKER distributions contain complementary and often more precise information on the fragmentation process than the broad diffuse absorption spectra. The distributions are calculated quantum mechanically for the diabatic state ${}^1A_2(\pi\sigma^*)$ either isolated or coupled to the ground electronic state at an exit channel conical intersection. The calculations use the novel ab initio quasi-diabatic potential energy matrix constructed in paper I. The approximate overlap integral-based adiabatic mapping approach is introduced with which the quantum mechanical TKER distributions can be efficiently and accurately reproduced. Finally, the calculated TKERs are compared with the experimental results. The main features of the measured vibrationally resolved distributions are reproduced, and the spectral peaks are assigned and interpreted in detail.

I. INTRODUCTION

This paper (paper II) continues the systematic analysis of the photochemistry of pyrrole (C_4H_4NH) in the first absorption band started in Ref. 1 (paper I). The absorption band is due to the two low lying $\pi\sigma^*$ states, ${}^1A_2(\pi\sigma^*)$ and ${}^1B_1(\pi\sigma^*)$, which are repulsive along the NH bond and form exit channel conical intersections (CIs) with the ground electronic state $\tilde{X}{}^1A_1(\pi\pi)$ [Fig. 1(a)]. The resulting topography of the state intersections is typical of many model biochromophores, and this study is motivated by the goal to clarify the impact

* Electronic mails: David.Picconi@ch.tum.de and david.picconi@gmail.com

† Electronic mails: Sergy.Grebenshchikov@ch.tum.de and sgreben@gwdg.de

of this topography on the observable features of the photodynamics. Paper I introduced the ab initio based full dimensional molecular Hamiltonian and analyzed the absorption spectra corresponding to the ultraviolet (UV) excitation of the first excited state ${}^1A_2(\pi\sigma^*)$ at wavelengths $\lambda \geq 240$ nm. Paper II focuses on the rovibrational product state and kinetic energy distributions of the pyrrolyl photofragment formed in its ground electronic state upon the light triggered H-atom elimination in the state ${}^1A_2(\pi\sigma^*)$. The preliminary results of the analysis of the CI $\tilde{X}/{}^1A_2(\pi\sigma^*)$ and its signatures in the product state distributions, in particular in the photofragment excitation spectra, are described in Ref. 2.

The photofragment distributions for the wavelengths λ between 254 nm and 240 nm, relevant for the present study, have been studied using the H-atom Rydberg tagging photofragment translational spectroscopy.³⁻⁵ The final state populations in these experiments are quantified in terms of the total kinetic energy release (TKER). In the two-fragment channel H + pyrrolyl, the TKER spectrum for a given photolysis wavelength is uniquely related to the rovibrational distribution of the pyrrolyl radical.^{3,4} The observed kinetic energy distributions consist of two well resolved components,³ a fast one (average kinetic energy $E_{\text{kin}} \geq 5000$ cm⁻¹) and a slow one ($E_{\text{kin}} \sim 1000$ cm⁻¹). Experimentalists associate the fast component with the direct dissociation occurring on a subpicosecond time scale of 20 fs — 110 fs,⁶⁻⁸ and the slow component with the statistical decomposition involving the ground electronic state and unfolding on the time scale of 1.1 ps.⁶

In this paper, we give a detailed description of the TKER spectra associated with the fast direct dissociation. In the long wavelength tail of the first absorption band, the experimental TKER spectra consist of merely several peaks indicating that only a limited number of vibrational states of pyrrolyl is selectively populated in the reaction.³ Ashfold and co-workers considered this result as an indication that pyrrole photodissociates in a vibrationally adiabatic fashion, with the modes orthogonal to the dissociation path preserving their initial vibrational excitation during the reaction. This vibrationally adiabatic mechanism was subsequently used to explain the TKER spectra observed in other model biochromophores.⁹

Several theoretical studies of the photofragment distributions in pyrrole have been published. Domcke and co-workers performed a quantum mechanical final state analysis using two- and three dimensional diabatic potentials and off-diagonal diabatic couplings.¹⁰ The primary goal was to investigate the dependence of the electronic branching ratios on the

initial vibrational state of the parent molecule. The formation of pyrrolyl was also studied using the classical mechanical ‘direct dynamics’ with all 24 degrees of freedom included.¹¹ The TKER and the angular distributions were calculated for the first four electronic states without the explicit construction of their potential energy surfaces, and the qualitative features of the low resolution TKER distributions measured by Stavros and co-workers⁷ were successfully reproduced.

To date, the high resolution TKER distributions of Refs. 3 and 4 have been neither analyzed theoretically nor accurately assigned. Furthermore, the extent of the vibrational adiabaticity in the photodissociation in the $\pi\sigma^*$ states remains unknown. This gap is closed in the present study which complements the analysis of the absorption spectra in paper I with the quantum mechanical calculations of the TKER distributions. The photofragment kinetic energy distributions measured by Ashfold and co-workers are of special significance for the theoretical studies: They are the only experimental data sets with high frequency resolution, which are available for the low lying $\pi\sigma^*$ states in pyrrole (the absorption cross sections could not be measured directly). These data sets serve as benchmarks for testing the quality of the constructed molecular Hamiltonian, the ab initio potential energy surfaces, and the quantum dynamics. In parallel, approximate quantum mechanical methods, which reduce the computational burden of the ab initio and the quantum dynamics steps, are introduced and tested. In paper I, the convolution approximation for the absorption spectra has been implemented as a tool to calculate and to assign the diffuse bands of the $\pi\sigma^*$ states. In paper II, we demonstrate that the exact photofragment distributions can be reproduced using the adiabatic mapping of the Franck-Condon (FC) excitations of the aromatic ring onto free fragment states. Both approximations work reliably for pyrrole and are expected to be generally applicable to the fast direct dissociation in $\pi\sigma^*$ states.

The paper is organized as follows: The form of the molecular Hamiltonian and the main results of paper I are recapitulated in Sect. II in order to keep the presentation self-contained. The quantum mechanical approach to the photofragment distributions using the MCTDH method¹² and the overlap integral-based mapping approximation are described in Sect. III and in the Appendix. In Sect. IV, the TKER spectra are discussed for the calculations in which six, eleven, and fifteen internal degrees of freedom are included. These are the same 6D, 11D, and 15D calculations, for which the absorption spectra in paper I were analyzed and assigned. The emphasis here is on the dissociation in the isolated state $1^1A_2(\pi\sigma^*)$. Conclu-

sions are given in Sect. V, complemented with a sketch of the non-adiabatic effects observed in the two-state dissociation dynamics of pyrrole in the electronic states $\tilde{X}/1^1A_2(\pi\sigma^*)$ weakly coupled at an exit channel conical intersection.

II. MOLECULAR HAMILTONIAN AND ABSORPTION SPECTRA

The molecular Hamiltonian, constructed in paper I for the electronic states \tilde{X} , A_2 , and B_1 in the locally diabatic representation [see Fig. 1(a)], is written as

$$\hat{\mathbf{H}} = \hat{T} \mathbf{1} + \begin{pmatrix} V^X & V^{XA_2} & V^{XB_1} \\ V^{XA_2} & V^{A_2} & V^{A_2B_1} \\ V^{XB_1} & V^{A_2B_1} & V^{B_1} \end{pmatrix}; \quad (1)$$

bold faced underlined characters denote 3×3 matrices. Pyrrole is described using (i) the ‘disappearing modes’, i.e. the three Jacobi coordinates $\mathbf{R} \equiv (R, \theta, \phi)$ of the dissociating H-atom defined relative to the center of mass of the pyrrolyl fragment and (ii) the ‘non-disappearing modes’, i.e. the 21 dimensionless normal modes \mathbf{Q} of the pyrrolyl ring. The normal modes \mathbf{Q} are partitioned into four symmetry blocks $\mathbf{Q} = \{\mathbf{Q}_{a_1}, \mathbf{Q}_{a_2}, \mathbf{Q}_{b_1}, \mathbf{Q}_{b_2}\}$. Examples of the normal modes in each symmetry block are given in Fig. 2. The kinetic energy operator in each diabatic state is written as a sum of the kinetic energies in the \mathbf{R} - and \mathbf{Q} -spaces, $\hat{T} = \hat{T}_R + \hat{T}_Q$, and the kinematic coupling between the disappearing modes and the vibrations of the ring is neglected.

The quasi-diabatic potential matrix \mathbf{V} in Eq. (1) is constructed as a sum of two terms,

$$\mathbf{V}(\mathbf{R}, \mathbf{Q}) = \mathbf{U}_R(\mathbf{R}) + \mathbf{W}_Q(\mathbf{Q}|R). \quad (2)$$

The term $\mathbf{U}_R(\mathbf{R})$ depends only on the disappearing modes (R, θ, ϕ) and is constructed by spline interpolations of the diabaticized ab initio energies on a dense ab initio three-dimensional (3D) grid in \mathbf{R} . The term $\mathbf{W}_Q(\mathbf{Q}|R)$ depends on the 21 non-disappearing modes \mathbf{Q} and on the interfragment distance R . The form of the matrix $\mathbf{W}_Q(\mathbf{Q}|R)$ is similar to the vibronic coupling model of Ref. 13 (i.e. the pyrrolyl ring is treated using quadratic Hamiltonians), but all model parameters are calculated with the CASPT2 method on a dense grid along R and subsequently interpolated. The off-diagonal diabatic matrix elements V^{XA_2} and V^{XB_1} in Eq. (2) are kept localized along the tuning mode R to the vicinities of the CIs

between states they refer to. They vanish outside the CI region (i.e. in the FC zone and in the dissociation channels) where the transition probability between states is negligible and where the adiabatic and the diabatic states are constructed to coincide.

The initial state of the parent molecule prior to photoexcitation is taken to be the ground vibrational state $\Psi_0(\mathbf{R}, \mathbf{Q})$ in the potential V^X of the ground electronic state \tilde{X} . Immediately after the photoexcitation, the molecule is in the state

$$\Phi_\epsilon(t=0) = (\boldsymbol{\mu}^{A_2}(\mathbf{R}, \mathbf{Q}) \cdot \hat{\epsilon}) \Psi_0(\mathbf{R}, \mathbf{Q}), \quad (3)$$

where $\hat{\epsilon} = x, y$ or z denotes the polarization vector of the electric field of the incident light and $\boldsymbol{\mu}^{A_2}(\mathbf{R}, \mathbf{Q})$ is the transition dipole moment (TDM) vector of the state $1^1A_2(\pi\sigma^*)$ with \tilde{X} . The molecular axes are chosen so that z runs along the NH bond, y lies in the ring plane, x is perpendicular to the ring plane, and all three are mutually orthogonal (see Fig. 2).

The state $1^1A_2(\pi\sigma^*)$ is optically dark, and the transition $1^1A_2(\pi\sigma^*) \leftarrow \tilde{X}$ becomes vibronically allowed upon displacements along the symmetry breaking modes of b_1 , b_2 , and a_2 symmetry. For this reason, the coordinate dependence of the TDMs in Eq. (3) is explicitly taken into account: This dependence materially affects the observed absorption spectra and the product state distributions in the $\pi\sigma^*$ states. The coordinate dependent TDM vector functions $\boldsymbol{\mu}^{A_2}(\mathbf{R}, \mathbf{Q})$ are written in the form

$$\boldsymbol{\mu}^{A_2}(\mathbf{R}, \mathbf{Q}) \approx \boldsymbol{\mu}_R^{A_2}(\mathbf{R}) + \boldsymbol{\mu}_Q^{A_2}(\mathbf{Q}|R). \quad (4)$$

consistent with the well-known Herzberg-Teller expansion.¹⁴ Two realizations of Eq. (4) are considered. One of them has the standard Herzberg-Teller form and includes only small deviations from the FC geometry, so that the TDM functions are strictly separable in \mathbf{R} and \mathbf{Q} :

$$\mu_x^{A_2}(\mathbf{R}, \mathbf{Q}) = \mu_{x,\theta}^{A_2}(R_{\text{FC}}) \sin(\theta) \sin(\phi) + \sum_i \mu_{x,i}^{A_2}(R_{\text{FC}}) Q_{b_2}(i), \quad (5a)$$

$$\mu_y^{A_2}(\mathbf{R}, \mathbf{Q}) = \mu_{y,\theta}^{A_2}(R_{\text{FC}}) \sin(\theta) \cos(\phi) + \sum_i \mu_{y,i}^{A_2}(R_{\text{FC}}) Q_{b_1}(i), \quad (5b)$$

$$\mu_z^{A_2}(\mathbf{R}, \mathbf{Q}) = \sum_i \mu_{z,i}^{A_2}(R_{\text{FC}}) Q_{a_2}(i). \quad (5c)$$

The sums run over all ring normal modes $Q_\Gamma(i)$ of the indicated symmetry Γ . The dependence on the disappearing angles is expressed in terms of the real spherical harmonics p_x and p_y . The intensity of excitation of a particular ring vibration $Q(i)$ in the state $1^1A_2(\pi\sigma^*)$

is proportional to the square of the Herzberg-Teller coefficient $\mu_{\epsilon,i}^{A_2}$. The numerical values of the coefficients are given in Table III of paper I. These TDMs were used in paper I in the calculations of the 6D, 11D, and 15D absorption spectra of the state $1^1A_2(\pi\sigma^*)$ [see Fig. 3(a–c)]. The analysis of the respective TKER distributions is given in Sect. IV.

A slightly different set of functions, which allows for a more realistic representation of the coordinate dependence of ab initio TDMs, is used to calculate TKER distributions which are compared with the experimental data of Ref. 3:

$$\mu_x^{A_2}(\mathbf{R}, \mathbf{Q}) = \mu_{x,\theta,1}^{A_2}(R) \sin \theta \sin \phi + \mu_{x,\theta,2}^{A_2}(R) \sin(2\theta) \sin \phi + \sum_i \mu_{x,i}^{A_2}(R) Q_{b_2}(i), \quad (6a)$$

$$\mu_y^{A_2}(\mathbf{R}, \mathbf{Q}) = \mu_{y,\theta,1}^{A_2}(R) \sin \theta \cos \phi + \mu_{y,\theta,2}^{A_2}(R) \sin(2\theta) \cos \phi + \sum_i \mu_{y,i}^{A_2}(R) Q_{b_1}(i), \quad (6b)$$

$$\mu_z^{A_2}(\mathbf{R}, \mathbf{Q}) = \sum_i \mu_{z,i}^{A_2}(R) Q_{a_2}(i). \quad (6c)$$

These functions are similar to the Herzberg-Teller expression of Eq. (5), with the following differences. First, the real spherical harmonics d_{xz} and d_{yz} are added to p_x and p_y to better describe the angular dependence of the TDMs. Second, the Herzberg-Teller coefficients are made R dependent via the second order Taylor expansion around the FC point R_{FC} :

$$\mu(R) = \mu^{(0)}(R_{\text{FC}}) + \mu^{(1)}(R_{\text{FC}}) (R - R_{\text{FC}}) + \mu^{(2)}(R_{\text{FC}}) (R - R_{\text{FC}})^2. \quad (7)$$

Finally, only the modes making the largest contributions to the TDM are kept in the Eq. (6). The expansion coefficients, found by fitting to the ab initio data, are summarized in Table I.

The photon energy dependent total absorption cross section is an incoherent average over the different electric field orientations,

$$\sigma_{\text{tot}}(\omega) = \frac{1}{3} \sum_{\epsilon=x,y,z} \sigma_{\epsilon}(E_{\text{ph}}). \quad (8)$$

Each cross section $\sigma_{\epsilon}(E_{\text{ph}})$ can be expressed as an expectation value¹⁵

$$\sigma_{\epsilon}(E_{\text{ph}}) = \frac{E_{\text{ph}}}{3c\epsilon_0} \lim_{\lambda \rightarrow 0} \lambda \langle \Psi_{\epsilon}^{\lambda}(\mathbf{Q}|E_{\text{ph}}) | \Psi_{\epsilon}^{\lambda}(\mathbf{Q}|E_{\text{ph}}) \rangle, \quad (9)$$

where the wave function $\Psi_{\epsilon}^{\lambda}(E_{\text{ph}})$ is a stationary energy component of $\Phi_{\epsilon}(t=0)$:

$$\Psi_{\epsilon}^{\lambda}(E_{\text{ph}}) = \hat{G}^+(E_{\text{ph}}) \Phi_{\epsilon}(t=0). \quad (10)$$

Here $\hat{G}^+(E)$ is the advanced Green's function,

$$\hat{G}^+(E_{\text{ph}}) = -i \int_0^\infty e^{-i(\hat{H}-i\lambda)t} e^{iE_{\text{ph}}t} dt, \quad (11)$$

for the state $1^1A_2(\pi\sigma^*)$ and λ in the above equations signifies the absorbing potential introduced at the edge of the coordinate grid. The quantum mechanical absorption spectra used in this work are shown in Fig. 3. They have smooth absorption envelopes modulated by the diffuse bands associated with excitations of the vibrational states in the shallow minimum of the state $1^1A_2(\pi\sigma^*)$ in the FC zone.

The quantum mechanical absorption spectrum for any polarization ϵ can be approximated by a convolution of the contributions due to the departing H-atom (in the space \mathbf{R} of the disappearing modes) and due to the pyrrolyl ring (in the space \mathbf{Q} of the ring modes). The convolution approximation was developed in paper I. First, the initial state of the parent molecule $\Psi_0(\mathbf{R}, \mathbf{Q})$ was replaced by a product of an \mathbf{R} - and a \mathbf{Q} -dependent factor, $\Psi_0(\mathbf{R}, \mathbf{Q}) \approx \Psi_R(\mathbf{R})\Psi_Q(\mathbf{Q})$. With the Herzberg-Teller TDMs, the photoexcited state $\Phi_\epsilon(t=0)$ was in the product form

$$\Phi_\epsilon(0) \approx F_R(\mathbf{R})f_Q(\mathbf{Q}), \quad (12)$$

or [e.g. in the case of the R -dependent Herzberg-Teller coefficients of Eq. (6)] in the sum-of-products form:

$$\Phi_\epsilon(0) \approx \sum F_R(\mathbf{R})f_Q(\mathbf{Q}). \quad (13)$$

Next, the diabatic potential of the state $1^1A_2(\pi\sigma^*)$, Eq. (2), was simplified into a sum of purely \mathbf{R} - and \mathbf{Q} -dependent terms, $V^{A_2} \approx U_R^{A_2}(\mathbf{R}) + W_Q^{A_2}(\mathbf{Q}|R_{\text{FC}})$, with the \mathbf{Q} -space term evaluated at a dissociation coordinate R fixed near R_{FC} in the FC zone. The molecular Hamiltonian was approximated by a separable expression:

$$\hat{H}_0 = \hat{T}_R + U_R^{A_2}(\mathbf{R}) + \hat{T}_Q + W_Q^{A_2}(\mathbf{Q}|R_{\text{FC}}) \equiv \hat{H}_R(\mathbf{R}) + \hat{H}_Q(\mathbf{Q}|R_{\text{FC}}). \quad (14)$$

With these two approximations, the absorption cross section assumed the form

$$\sigma(E_{\text{ph}}) = \frac{E_{\text{ph}}}{2\epsilon_0 c} \int_{-\infty}^\infty \bar{\sigma}_R(E_{\text{ph}} - \omega) \bar{\sigma}_Q(\omega) d\omega, \quad (15)$$

where the 'spectral functions' $\bar{\sigma}_R$ and $\bar{\sigma}_Q$ (i.e. the cross sections without energy prefactors) were calculated separately for the disappearing modes and for the pyrrolyl ring. The function $\bar{\sigma}_R$ is a smooth almost structureless envelope corresponding to the fast direct dissociation

in the repulsive $\pi\sigma^*$ state. The function $\bar{\sigma}_Q$ consists of a series of δ -peaks of vibrational excitations in a bound-bound transition. For the vibronic coupling model, in which the Hamiltonian of the heteroaromatic ring is represented as a set of coupled harmonic oscillators, the factor $\bar{\sigma}_Q(E)$ is simply a FC spectrum. If the photoexcited state has a simple product form of Eq. (12), the spectrum $\bar{\sigma}_Q(E)$ is given by the overlap integrals,

$$\bar{\sigma}_Q(E) = \sum_{\mathbf{m}} |\langle \varphi_{\mathbf{m}}(\mathbf{Q}) | f_Q(\mathbf{Q}) \rangle|^2 \delta(E - E_{\mathbf{m}}), \quad (16)$$

between the eigenfunctions $\varphi_{\mathbf{m}}(\mathbf{Q})$ of the ring modes in the FC zone (with energies $E_{\mathbf{m}}$ and the vector of the quantum numbers \mathbf{m}), and the initial state f_Q . For the sum-of-products form of Eq. (13), the final expressions, derived in paper I, are slightly more involved.

The convolution approximation for the H-atom elimination reactions substantially reduces the computational effort required to construct the molecular Hamiltonian and to calculate the absorption spectrum. Indeed, the explicit construction of the potential energy surfaces and the numerical solution of the nuclear Schrödinger equation are restricted to the space of the three disappearing modes regardless of the actual size of the biochromophore. The good accuracy of the convolution approximation was demonstrated in paper I. It is also a convenient starting point for the overlap integral-based approach to the photofragment distributions discussed in Sect. III B.

III. PHOTOFRAGMENT DISTRIBUTIONS

A. Quantum mechanical calculations

The quantum mechanical calculations of the rovibrational photofragment distributions in the electronic channel H + pyrrolyl(2A_2), diabatically correlating with the state $1^1A_2(\pi\sigma^*)$, are performed using the projection method of Balint-Kurti and coworkers,^{16,17} which is formulated here in the time-independent framework.^{15,18,19} The partial photodissociation cross section for the formation of pyrrolyl in a final vibrational state \mathbf{n} is given by:^{15,17}

$$\sigma(E_{\text{ph}}, \mathbf{n}) = \frac{E_{\text{ph}}}{3c\epsilon_0} \lim_{\lambda \rightarrow 0} \lambda |\langle \psi_{\mathbf{n}}^- | \Psi^\lambda(E_{\text{ph}}) \rangle|^2 = \frac{E_{\text{ph}}}{3c\epsilon_0} |T_{\mathbf{n}}(E_{\text{ph}})|^2; \quad (17)$$

the index ϵ indicating the polarization direction of the incident light is omitted; the rotations of pyrrolyl and the quantum numbers of the associated coordinates θ and ϕ are not explicitly included here, although they are taken into account in the actual calculations.²⁰ The

scattering state $\psi_{\mathbf{n}}^-(E_{\text{ph}})$ in the dissociation continuum describes the atom and the radical with photon energy E_{ph} recoiling into the channel \mathbf{n} . The energy resolved state $\Psi^\lambda(E_{\text{ph}})$ is defined in Eq. (10). At large pyrrolyl—H distances $R \rightarrow \infty$, it contains purely outgoing waves along R :

$$\Psi^\lambda(E_{\text{ph}}) \xrightarrow{R \rightarrow \infty} - \sum_{\mathbf{n}} T_{\mathbf{n}}(E_{\text{ph}}) \sqrt{\frac{m_R}{k_{\mathbf{n}}}} e^{ik_{\mathbf{n}}R} \chi_{\mathbf{n}}(\mathbf{Q}). \quad (18)$$

The wave functions $\chi_{\mathbf{n}}(\mathbf{Q})$ are the vibrational eigenstates of pyrrolyl with energies $E_{\mathbf{n}}$ and $k_{\mathbf{n}} = \sqrt{2m_R(E_{\text{ph}} - E_{\mathbf{n}})}$ is the channel momentum;²⁰ $m_R \approx m_H$ is the pyrrolyl/H reduced mass. The amplitudes in each channel are the photodissociation matrix elements $T_{\mathbf{n}}(E_{\text{ph}})$ which thus contain the dynamical information on the dissociation process.¹⁷ The T -matrix elements are found by introducing the projection operators

$$\hat{\mathcal{P}}_{\mathbf{n}} = \delta(R - R_\infty) |\chi_{\mathbf{n}}(\mathbf{Q})\rangle. \quad (19)$$

The operators $\hat{\mathcal{P}}_{\mathbf{n}}$ act in the \mathbf{Q} -space and project onto $\chi_{\mathbf{n}}$ at the analysis line $R = R_\infty$ located in the asymptotic region. An application to the state $\Psi^\lambda(E)$ gives:

$$|T_{\mathbf{n}}(E_{\text{ph}})|^2 \sim \frac{k_{\mathbf{n}}}{m_R} \left| \langle \hat{\mathcal{P}}_{\mathbf{n}}^* | \Psi^\lambda(E_{\text{ph}}) \rangle \right|^2. \quad (20)$$

The matrix elements $|T_{\mathbf{n}}(E_{\text{ph}})|^2$ are, with a proper normalization, the vibrational photofragment distributions. Summation of the partial cross sections over all quantum numbers \mathbf{n} gives the total absorption cross section of Eq. (9). The TKER spectrum^{3,5} $I_{\text{TKER}}(E_{\text{kin}}|E_{\text{ph}})$ is obtained via transforming the internal energy distributions to the photofragment kinetic energy scale:

$$I_{\text{TKER}}(E_{\text{kin}}|E_{\text{ph}}) = \sum_{\mathbf{n}} |T_{\mathbf{n}}(E_{\text{ph}})|^2 \delta(E_{\text{ph}} - E_{\mathbf{n}} - E_{\text{kin}}). \quad (21)$$

Thus, each peak in the TKER spectrum corresponds to a vibrational state of the pyrrolyl fragment populated during photodissociation. The vibrational energies $E_{\mathbf{n}}$ in the above expression are defined relative to the ground vibrational state of the ground electronic state \tilde{X} ; in this scale, the energy of the lowest channel E_0 is exactly the quantum mechanical dissociation threshold D_0 . The practical calculation of the photofragment distributions using the MCTDH program package is outlined in the Appendix.

B. Overlap integral-based mapping calculations of the photofragment distributions

The T -matrix elements and the photofragment distributions can be calculated approximately by means of the overlap integral-based mapping. The approach can be illustrated using the convolution method for the absorption spectra, introduced in paper I and sketched in Sect. II. The convolution of the spectral functions in Eq. (15), is valid for the Green's functions as well.²¹

$$\hat{G}^+(E_{\text{ph}}) \approx \hat{G}_0^+(E_{\text{ph}}) = -(2\pi i)^{-1} \int_{-\infty}^{\infty} \hat{G}_R^+(E_{\text{ph}} - \omega) \hat{G}_Q^+(\omega) d\omega. \quad (22)$$

The Green's function $\hat{G}_R^+(E) = (E - \hat{H}_R(\mathbf{R}) + i\lambda)^{-1}$ refers to the \mathbf{R} space of three disappearing modes. The vibrational spectrum of the pyrrolyl normal modes is discrete [cf. Eq. (16)], and the \mathbf{Q} space Green's function $\hat{G}_Q^+(E) = (E - \hat{H}_Q(\mathbf{Q}|R_{\text{FC}}) + i\lambda)^{-1}$ can be represented as a sum over the vibrational states. The convolution integral can therefore be rewritten as

$$\hat{G}_0^+(E_{\text{ph}}) = \sum_{\mathbf{m}} \hat{G}_R^+(E_{\text{ph}} - E_{\mathbf{m}}) |\varphi_{\mathbf{m}}\rangle \langle \varphi_{\mathbf{m}}|, \quad (23)$$

where index \mathbf{m} numbers the eigenstates $\varphi_{\mathbf{m}}$ of the ring in the FC zone. Applying the Green's function \hat{G}_0^+ to the initial state $\Phi(t=0)$ gives an approximation to the stationary energy component $\Psi^\lambda(E_{\text{ph}})$. For the initial state in the simple product form, $\Phi(0) = F_R f_Q$ [cf. Eq. (12)], one finds

$$\Psi^\lambda(E_{\text{ph}}) \approx \hat{G}_0^+(E_{\text{ph}}) \Phi(0) = \sum_{\mathbf{m}} \left[\hat{G}_R^+(E_{\text{ph}} - E_{\mathbf{m}}) F_R(\mathbf{R}) \right] \langle \varphi_{\mathbf{m}} | f_Q \rangle \varphi_{\mathbf{m}}(\mathbf{Q}). \quad (24)$$

The Green's function $\left[\hat{G}_R^+ F_R \right]$ acting on the initial state in the \mathbf{R} space generates outgoing waves along R for each vibrational state of the ring initially excited with the amplitude $\langle \varphi_{\mathbf{m}} | f_Q \rangle$. Although the above derivation uses separability of the Hamiltonian near R_{FC} , the form of $\Psi^\lambda(E_{\text{ph}})$, in particular the expansion in the ring states, is approximately valid for larger R along the dissociation path. The requirement is that the eigenstates $\varphi_{\mathbf{m}}(\mathbf{Q})$ vary smoothly along the dissociation coordinate and commute with the kinetic energy \hat{T}_R . This implies an adiabatic evolution in the coordinates orthogonal to the reaction path: As interfragment distance grows, the states $\varphi_{\mathbf{m}}$ with energies $E_{\mathbf{m}}$ very gradually turn into the vibrational states of the free pyrrolyl $\chi_{\mathbf{n}}$ with energies $E_{\mathbf{n}}$, $(E_{\mathbf{m}}, \varphi_{\mathbf{m}}) \xrightarrow{R \rightarrow \infty} (E_{\mathbf{n}}, \chi_{\mathbf{n}})$. For large R , the adiabatic state $\Psi^\lambda(E_{\text{ph}})$ of Eq. (24) is in the channel form of Eq. (18):

$$\Psi^\lambda(E_{\text{ph}}) \xrightarrow{R \rightarrow \infty} - \sum_{\mathbf{n}} [\bar{\sigma}_R(E_{\text{ph}} - E_{\mathbf{n}})]^{1/2} e^{i\alpha_R} \langle \varphi_{\mathbf{m}} | f_Q \rangle \sqrt{\frac{m_R}{k_{\mathbf{n}}}} e^{ik_{\mathbf{n}}R} \chi_{\mathbf{n}}(\mathbf{Q}), \quad (25)$$

where $[\bar{\sigma}_R(E_{\text{ph}} - E_n)]^{1/2} e^{i\alpha_R}$ stands for the complex amplitude of the outgoing wave of $[\hat{G}_R^+ F_R]$ along the reaction coordinate in a given channel \mathbf{n} . Application of the projector $\hat{\mathcal{P}}_{\mathbf{n}}$ gives the vibrational state distributions in the mapping approximation:

$$|t_{\mathbf{n}}(E_{\text{ph}})|^2 \sim \frac{k_{\mathbf{n}}}{m_R} |\langle \varphi_{\mathbf{m}}(\mathbf{Q}) | f_Q(\mathbf{Q}) \rangle|^2 \bar{\sigma}_R(E_{\text{ph}} - E_n). \quad (26)$$

They are proportional to the FC overlap integrals in the \mathbf{Q} space, taken at the excitation point R_{FC} and weighted with the ‘radial factor’ $\bar{\sigma}_R = \lim_{\lambda \rightarrow 0} \lambda \langle \hat{G}_R^+ F_R | \hat{G}_R^+ F_R \rangle$. The physical interpretation in view of Eq. (16) is that the population of a given product state $\chi_{\mathbf{n}}$ is controlled by the intensity $|\langle \varphi_{\mathbf{m}} | f_Q \rangle|^2$ of excitation of the adiabatically connected state $\varphi_{\mathbf{m}}$ in the FC zone, multiplied by the probability $\bar{\sigma}_R(E_{\text{ph}} - E_n)$ of excitation of the radial dissociative motion with the translational energy $E_{\text{kin}} = E_{\text{ph}} - E_n$.²² In other words, the harmonic populations of the non-disappearing modes in the FC zone are adiabatically translated to the infinite interfragment separation and mapped onto adiabatically connected product states. In the adiabatic regime, the dissociation dynamics in the \mathbf{R} space unfolds on the adiabatic potentials $E_{\mathbf{m}}(\mathbf{R})$. These are shown in Fig. 1(f) for the ring modes of a_1 symmetry. They are constructed by diagonalizing the Hessian matrix of the ring modes for a set of R values, and calculating the harmonic energies of one-quantum excitations in each mode. The adiabatic curves are almost strictly parallel to each other, implying small non-adiabatic derivative couplings and the prevailing adiabatic (i.e. the ‘Born-Oppenheimer’) evolution along the vibrational curves. Several avoided crossings between the curves mark NH distances at which the residual vibrational energy exchange takes place.

In the actual application of the adiabatic mapping approximation, each normal mode in the FC region is associated with the pyrrolyl mode with the largest squared Duschinsky overlap. In this way, a one-to-one mapping is defined between the quantum numbers \mathbf{m} of the FC modes and the quantum numbers \mathbf{n} of the free pyrrolyl modes (which is equivalent to the mapping between the wavefunctions $\varphi_{\mathbf{m}} \rightarrow \chi_{\mathbf{n}}$).

The expression for the product state distributions in the overlap integral-based adiabatic mapping looks similar to the semiclassical FC mapping expression familiar in the context of the triatomic photodissociation (see, for example, Refs. 23–25). The FC mapping is recovered if the spectral amplitudes $\langle \varphi_{\mathbf{m}} | f_Q \rangle$ are replaced with the projections $\langle \chi_{\mathbf{n}} | f_Q \rangle$ of the initial wave function directly onto the asymptotic product states. Test calculations demonstrated, however, that the FC mapping is not accurate for pyrrole.

The adiabatically mapped final state distributions can also be constructed for an initial state of Eq. (13), i.e. for $\Phi(0) = \sum F_R f_Q$. Now several terms $[\hat{G}_R^+ F_R]$ generate outgoing waves with amplitudes $[\bar{\sigma}_R(E_{\text{ph}} - E_{\mathbf{n}})]^{1/2} e^{i\alpha_R}$, and the T -matrix elements are given by

$$|t_{\mathbf{n}}(E_{\text{ph}})|^2 \sim \frac{k_{\mathbf{n}}}{m_R} \left| \sum \langle \varphi_{\mathbf{m}}(\mathbf{Q}) | f_Q(\mathbf{Q}) \rangle \bar{\sigma}_R(E_{\text{ph}} - E_{\mathbf{n}})^{1/2} e^{i\alpha_R} \right|^2. \quad (27)$$

Although the form of Eq. (27) is less transparent, the calculation remains straightforward. The complex amplitudes for each F_R can be reconstructed, for example, using the projection method of Balint-Kurti applied in the dissociative \mathbf{R} space.

Equations (26) and (27) are the main result of this section. The actual implementation of them involves three main steps: First, the spectral function $\bar{\sigma}_R$ (or the wave amplitudes $[\dots]^{1/2} e^{i\alpha_R}$) are calculated by solving the 3D Schrödinger equation in the \mathbf{R} space. Second, the overlap integrals $\langle \varphi_{\mathbf{m}}(\mathbf{Q}) | f_Q(\mathbf{Q}) \rangle$ are determined for the ring modes in the FC zone. Finally, the mapping between the modes in the FC zone and in the asymptotic region, $\varphi_{\mathbf{m}} \rightarrow \chi_{\mathbf{n}}$, is established. With the input produced in these three steps, the T -matrix elements $|t_{\mathbf{n}}(E_{\text{ph}})|^2$ are found, and the TKER spectrum is calculated using Eq. (21).

IV. RESULTS

A. Quantum mechanics versus adiabatic mapping

The TKER spectra of the recoiling $\text{C}_4\text{H}_4\text{N}$ and H are evaluated for the 6D, 11D, and 15D absorption spectra. The spectra calculated using the Herzberg-Teller TDMs of Eq. (5) are shown in Fig. 3. The 6D and 11D calculations are performed for the isolated electronic state 1^1A_2 , with the non-totally symmetric modes b_1 (for 6D) and all totally symmetric modes a_1 (for 11D) dynamically active. The 15D calculation is performed for the coupled pair \tilde{X}/A_2 . It includes all modes of a_2 and b_1 symmetry, three a_1 modes with the largest displacement between the minima of pyrrole and pyrrolyl, as well as three b_2 modes along which the Herzberg-Teller coefficients of the TDMs are the largest. The parameters of all MCTDH calculations are summarized in Table VI of paper I.

The individual states in the TKER spectra have translational energies $E_{\text{kin}} = E_{\text{ph}} - E_{\mathbf{n},j,k}$ where $E_{\mathbf{n},j,k}$ is the internal energy of pyrrolyl which is measured with respect to the ground vibrational state in \tilde{X} and includes the energy of the final rotational state (j, k) .²⁰ Example of the rotational state distribution, calculated for the 3D potential of the disappearing

modes, is shown in Fig. 4(a). The rotational excitation is at best modest: The rotational states of pyrrolyl with $j \leq 25$ are populated. The reason for this is the weak torque along θ experienced by the dissociating wave packet. The maximum is reached at $j = 10$, corresponding to the rotational energy of merely 30.6 cm^{-1} , and the full width at half maximum (FWHM) is near 60 cm^{-1} . This is in agreement with the observation of Cronin et al. that the product $\text{C}_4\text{H}_4\text{N}$ is formed rotationally cold.³ In the vibrational distributions discussed below, the rotational structure is not resolved: The δ -function in Eq. (21) is replaced with a Gaussian with a standard deviation of 10 cm^{-1} , and the narrowly spaced rotational states are merged into a single peak profile.

1. *6D product state distributions: Coordinates $R, \theta, \phi, Q_{b_1}(1, 2, 3)$*

In this calculation the ${}^1A_2 \leftarrow \tilde{X}$ excitation is induced by the TDM components μ_x and μ_y (see paper I for the detailed discussion). The x -polarized transition leads to the formation of pyrrolyl in the vibrational states belonging to the irrep a_1 (associated with rotational states of b_2 symmetry). The y -polarized transition excites either the disappearing out-of-plane H-atom bending (irrep b_1) or the ring normal modes of b_1 symmetry. If the disappearing bending is excited, pyrrolyl is formed in the a_1 vibrational states and b_1 rotational states. If the ring modes are excited, pyrrolyl is formed in the b_1 vibrational states and a_1 rotational states. These symmetry considerations are useful and straightforward. In our calculations, they hold because the calculations are performed for the zero total angular momentum in a single electronic state and because the harmonic Hamiltonian for the \mathbf{Q} space, based on the block diagonal Hessian, prevents the energy exchange between the degrees of freedom belonging to different irreps.

The TKER distributions calculated using the MCTDH and the mapping approach are illustrated in Fig. 5 for the excitation energies $E_{\text{ph}} = 4.1 \text{ eV}$ and $E_{\text{ph}} = 4.3 \text{ eV}$, corresponding to the maximum and the shoulder of the spectrum in Fig. 3(a). The TKER spectra, averaged over the field polarizations, consist of three peaks. Their rotational width, $\text{FWHM} \approx 60 \text{ cm}^{-1}$, is the same as for the distribution calculated for the 3D case and shown in Fig. 4(a). For the case of MCTDH, the rovibrational populations are calculated directly. For the case of mapping, the rovibrational populations are evaluated as $|t_{\mathbf{n}}(E_{\text{ph}})|^2 P_{j,k}$, with the unity normalized rotational populations $P_{j,k}$ calculated for the dissociation in the \mathbf{R}

space at the maximum of the $\bar{\sigma}_R$ profile.

The assignment of the peaks is easier to clarify first using the mapping calculation. Indeed, from the convolution calculation of the absorption spectrum, we know the assignment of each absorption band in terms of the ring excitations in the FC zone (see paper I). Moreover, the mapping of each such ring excitation onto free pyrrolyl is also known and Fig. 1(c), showing the adiabatic frequencies of the b_1 ring modes as functions of R , provides an illustration of this mapping. For $E_{\text{ph}} = 4.1$ eV [Fig. 5(a)], the fastest peak corresponds to the vibrational ground state $\mathbf{0}$ (labeled 1 in the combs in Fig. 5), and the two slower peaks are the fundamental excitations of the modes $Q_{b_1}(2)$ ($n_{b_1}(2) = 1$; label 2) and $Q_{b_1}(3)$ ($n_{b_1}(3) = 1$; label 3) excited by the TDM component μ_y . The intensity of the mode $Q_{b_1}(1)$ is negligible because the corresponding Herzberg-Teller coefficient in the TDM expansion is small. The TKER calculated using MCTDH has very similar intensities on the same pyrrolyl states. For the 6D potential V^{A_2} , involving only symmetry breaking ring modes, the dynamics is vibrationally adiabatic. The adiabatic frequency curves in Fig. 1(c) confirm this conclusion: They are well separated and free from avoided crossings. Therefore the initial vibrational state distribution of the ring vibrations, created during the optical excitation, is carried over to the fragments without much energy redistribution.

In their experimental study, Ashfold and co-workers argued that the significant intensity observed for the ground vibrational state of pyrrolyl was due to vibrationally non-adiabatic effects.³ The present calculations show that this state is formed because the TDM components μ_x and μ_y excite the in- and out-of-plane bending modes of the detaching H-atom which evolve adiabatically into the free rotations of vibrationless pyrrolyl. For the higher photon energy, $E_{\text{ph}} = 4.3$ eV [Fig. 5(b)], the TKER peaks shift to higher kinetic energies but the pattern remains the same. This is in agreement with the assignment¹ of the shoulder band of the 6D absorption spectrum to the same ring states as the main absorption band plus one quantum of the NH stretch excitation, $n_R = 1$. This excitation corresponds to a disappearing mode, and leaves no peaks in the TKER. The color of the assignment combs is meant to stress this observation: For the peaks originating from absorption bands with a given ring excitation and the lowest possible excitation in the disappearing modes ($n_R = 0$ in this case), the combs are shown red; for the peaks stemming from the absorption bands with the same ring excitation plus an additional excitation of the disappearing modes ($n_R = 1$), the combs are blue.

The TKER peaks corresponding to a given pyrrolyl excitation and observed over a broad range of photon energies are repeatedly found in the calculations described below. The peaks merely shift to higher kinetic energies with growing E_{ph} but do not disappear. The origin of this observation is related to the characteristic excitation pattern in the absorption spectra discussed in paper I: Many absorption bands above the ground state in the local minimum of the state $1^1A_2(\pi\sigma^*)$ carry multiple assignments which include ring excitations already observed in the low lying bands augmented with additional quanta in the disappearing modes.¹

2. *11D product state distributions: Coordinates R, θ, ϕ, Q_{a_1} (1, 2, 3, 4, 5, 6, 7, 8)*

In the 11D calculation, two TDM components μ_x and μ_y mediate the $1^1A_2 \leftarrow \tilde{X}$ transition; two TKER spectra $I_{\text{TKER},x,y}(E_{\text{kin}}|E_{\text{ph}})$ are observed while the component $I_{\text{TKER},z}(E_{\text{kin}}|E_{\text{ph}})$ vanishes. The transition excites exclusively the in- and out-of-plane H bending modes. Since the initially excited coordinates are disappearing modes, pyrrolyl is formed in the vibrational states of a_1 symmetry (including the ground vibrational state $\mathbf{0}$), associated with rotational states of either b_2 or b_1 symmetry.

The polarization averaged TKER profiles,

$$I_{\text{TKER}}(E_{\text{kin}}|E_{\text{ph}}) = \frac{1}{3} [I_{\text{TKER},x}(E_{\text{kin}}|E_{\text{ph}}) + I_{\text{TKER},y}(E_{\text{kin}}|E_{\text{ph}}) + I_{\text{TKER},z}(E_{\text{kin}}|E_{\text{ph}})],$$

corresponding to the specific absorption bands in the spectrum in Fig. 3(b), are plotted in Fig. 6 for the excitation energies of $E_{\text{ph}} = 4.40$ eV, $E_{\text{ph}} = 4.65$ eV, and $E_{\text{ph}} = 4.80$ eV (diffuse bands A, D and F). A number of vibrational peaks are visible in each TKER spectrum. Their rotational line shapes are very similar to the 6D case.

The vibrational states of pyrrolyl, populated in the TKER spectra, clearly change with the photon energy. As one moves from the absorption band A to D to F, the spectral patterns in TKER become noticeably richer. This is different from the 6D case, and in agreement with our understanding that the consecutive bands in the absorption spectrum in Fig. 3(b) are dominated by excitations of different ring modes. Note however that the spectral patterns get ‘enriched’ rather than replaced. Of course, the TKER spectrum calculated for a given absorption band carries excitations unique to this band. However, the excitations already observed at lower energies are still visible albeit with lower intensity. The inheritance of

the spectral patterns is related to the excitations of the disappearing modes in the FC zone. The assignments of the major TKER peaks, marked with combs in Fig. 6 and consecutively labeled through all three panels, are summarized in Table II.

The excitation energy of $E_{\text{ph}} = 4.40 \text{ eV}$ [panel (a)] is close to the spectral origin, i.e. the absorption band A. This band is due to the excitations of the disappearing bending modes, has zero NH stretch excitation ($n_R = 0$), and the TKER obtained via mapping consists of a single rotationally broadened peak of the ground vibrational state $\mathbf{0}$ of pyrrolyl (label 1; cf. Table II). This is also the dominant peak in the TKER distribution calculated using MCTDH. However, the photodissociation is not strictly vibrationally adiabatic, and another state with a one quantum excitation of the low frequency mode $Q_{a_1}(1)$, $n_{a_1}(1) = 1$, is also populated in the quantum mechanical TKER (label 2); this peak is not linked to an absorption band in Table II. There are two clear indications of the vibrational non-adiabaticity of the mode $Q_{a_1}(1)$. While not much displaced in the FC zone, it is the most displaced mode between pyrrole and pyrrolyl. As a consequence, the $Q_{a_1}(1)$ mode develops an excitation along the dissociation pathway, away from the FC zone. Second, its frequency plotted against the NH stretching mode R in Fig. 1(b) shows an avoided crossing with the adiabatic frequency curve for the mode $Q_{a_1}(2)$ near $R \sim 4.2 a_0$. The states with excitations residing on the higher frequency modes have low initial intensities, and their populations are negligible.

The energy $E_{\text{ph}} = 4.65 \text{ eV}$ corresponds to the absorption band D, and the TKER spectra are substantially enriched [panel (b)]. In the TKER obtained via mapping, the dominant peaks are 3, 4, and 6, as well as 10 and 11. As indicated in Table II, the first three are one quantum excitations of the pyrrolyl modes $Q_{a_1}(2)$, $Q_{a_1}(3)$, and $Q_{a_1}(5)$. The last two are due to a two-quantum excitation and a combination state. The ring excitation $n_{a_1}(5) = 1$, augmented with the obligatory fundamental bending excitations and $n_R = 0$, is one of the main contributors to the absorption peak D. The two other ring states, $n_{a_1}(2) = 1$ and $n_{a_1}(3) = 1$, if combined with the obligatory bending excitations stem from the absorption band B lying $\sim 0.14 \text{ eV}$ below the band D. As discussed in paper I, the ring states are ‘transposed’ to the higher lying absorption band via the additional excitation of the disappearing NH bending ($n_\theta = 3$) in the FC zone. Note that even in the ‘simple’ case of the adiabatic mapping, the assignment of the TKER spectra in 11D is complicated, and several additional minor peaks can actually be resolved. Strictly speaking, all corresponding

ring excitations could have been listed as (minor) components of the absorption band D.

The quantum mechanical TKER are similar in many respects, and most states predicted in the mapping calculations are populated, although not always with the same intensities. For the peaks 3 and 6, the MCTDH intensities are similar to those predicted by mapping, while the MCTDH intensities of the peaks 10 and 11 are noticeably lower. The discrepancies between MCTDH and mapping are indicative of the vibrationally non-adiabatic photodissociation. A case in point is provided by the peaks 4 ($n_{a1}(3) = 1$; absent in the quantum mechanical TKER) and 5 ($n_{a1}(4) = 1$; absent in the mapping TKER). The ring modes $\tilde{Q}_{a1}(4)$ and $\tilde{Q}_{a1}(3)$ undergo a strong Duschinsky mixing as the distance $\text{C}_4\text{H}_4\text{N}\cdots\text{H}$ grows across the FC zone. This is also seen in the adiabatic frequency curves for these two modes in Fig. 1(b), which exhibit an avoided crossing for $R \approx 4.0 a_0$ and $4.3 a_0$. In the mapping calculation, the asymptotic pyrrolyl mode $Q_{a1}(3)$ is mapped only on one mode of this pair, namely $\tilde{Q}_{a1}(3)$, and only a part of the true TKER distribution is recovered.

The peaks 1 and 2, inherited from the absorption band A are clearly visible, too. The corresponding combs are shown with blue color in panel (b). Thus, the ground vibrational state of the ring contributes to the assignment of the high energy band D. This is again realized via excitation of the disappearing mode, in this case the NH stretch (the anharmonic frequency of $\sim 2100 \text{ cm}^{-1}$), possibly accompanied by an additional low frequency bending excitation. Such moderate excitations of the disappearing modes are collectively marked as $n_R = 1$ in Table II and in Fig. 6.

The TKER distribution for $E_{\text{ph}} = 4.80 \text{ eV}$, corresponding to the absorption peak F, illustrates the further development of the above trends [panel (c)]. Again, several groups of TKER peaks can be distinguished. The peaks 14 — 18, shown with red, correspond to $n_R = 0$ and a weak bending excitation. The assignment of these peaks, given in Table II, shows that all of them are combination bands. Note that two of these ring states are first encountered in the absorption band E located slightly below F. The peaks indicated with the blue comb are inherited from the absorption band D. The corresponding pyrrole states in the FC zone carry the same labels in the \mathbf{Q} space, and an additional excitation in the \mathbf{R} space symbolically denoted $n_R = 1$. Finally, the gray comb marks the weak contribution of states inherited from the low lying band A which in the FC zone possess, along with the ring excitations shown in Table II, a strong excitation $n_R = 2$ of the disappearing modes.

The adiabatic mapping is seen to give reliable predictions of the TKER distributions

across the broad photon energy range. In the case of the a_1 ring modes, strongly coupled to each other and to the dissociation coordinate, the accuracy of the mapping calculations is the highest for the one quantum excitations. For the large amplitude combination states, the vibrationally non-adiabatic effects become prominent as the effective intramode coupling grows. As illustrated in Fig. 1(b), the avoided crossings between adiabatic curves and the associated intramode mixings are restricted to short distances $R \leq 4.5 a_0$.

3. 15D product state distributions: Coordinates

$$R, \theta, \phi, Q_{a_1}(1, 2, 5), Q_{a_2}(1, 2, 3), Q_{b_1}(1, 2, 3), Q_{b_2}(1, 3, 5)$$

The normal modes of pyrrolyl included in this 15D calculation are sketched in Fig. 2. The quantum mechanical TKER spectra are calculated for the coupled states ${}^1A_2/\tilde{X}$ and shown in Fig. 7 for the excitation energies $E_{\text{ph}} = 4.35 \text{ eV}$, $E_{\text{ph}} = 4.50 \text{ eV}$ and $E_{\text{ph}} = 4.65 \text{ eV}$, corresponding to the diffuse bands A, C and D in Fig. 3(c). The assignments of the kinetic energy peaks are listed in Table III. The internal conversion $A_2 \rightarrow \tilde{X}$ involves less than 10% of the initial population,² and the non-adiabatic two-state effects are localized to narrow vicinities of the excitation energies corresponding to Fano resonances. Our TKERs are calculated at a set of fixed photon energies, i.e. in the same way as the experiments are often conducted,⁵ and Fano resonances mostly pass unnoticed. For this reason, the mapping calculations are performed for the single state ${}^1A_2(\pi\sigma^*)$. The impact of Fano interference on the product state distributions is illustrated in Sect. V using PHOFEX spectra.

The ${}^1A_2 \leftarrow \tilde{X}$ transition is induced by the three TDM components, which create three different initial states, and are associated with product states of different symmetries. The final state symmetry is an attribute which can considerably simplify the assignment of the TKER peaks. The irrep of the fragment vibrational-rotational states is given as the direct product $\Gamma_Q \times \Gamma_{\text{ang}}$, where Γ_Q and Γ_{ang} are the irreps of the vibrational and rotational eigenfunctions, respectively. For the μ_x -induced transition, the symmetry allowed vibrational-rotational states have b_2 symmetry which we find realized in the combinations (i') ($\Gamma_Q = a_1$, $\Gamma_{\text{ang}} = b_2$) and (ii) ($\Gamma_Q = b_2$, $\Gamma_{\text{ang}} = a_1$). For the μ_y -induced transition, the total symmetry is b_1 which in the calculations is found as (i'') ($\Gamma_Q = a_1$, $\Gamma_{\text{ang}} = b_1$) and (iii) ($\Gamma_Q = b_1$, $\Gamma_{\text{ang}} = a_1$). Finally, for the μ_z -induced transition the total symmetry is a_2 which is found realized via the combination (iv) ($\Gamma_Q = a_2$, $\Gamma_{\text{ang}} = a_1$).²⁶ An example of the TKER

distribution broken down into the four symmetry blocks (i)—(iv) is given in Fig. 8.

For $E_{\text{ph}} = 4.35 \text{ eV}$ [panel (a)], the TKER spectrum is dominated by the pyrrolyl fragments in the ground vibrational state (Table III). The absorption band A is primarily due to the vibrational states having one quantum of the disappearing bending excitations. This is clearly reflected in both the mapping and the quantum mechanical TKER distributions. The vibrational states with no bending excitation and one quanta along the modes $\tilde{Q}_{a_2}(2, 3)$ and $\tilde{Q}_{b_1}(2, 3)$ also make significant contributions to the absorption band A. These are also found in the mapping TKER (which is expected) and in the quantum mechanical TKER (which indicates that the photodissociation follows the vibrationally adiabatic mechanism). The contributions to the TKER spectra arising from the pyrrolyl states belonging to a specific irrep of the C_{2v} point group are illustrated in Fig. 8. The pyrrolyl states of a_1 symmetry originate from the excitation of the disappearing bending vibrations in the x - and y -polarized transitions. Several TKER peaks in Fig. 7, Fig. 8, and in Table III carry multiple assignments. Such are, for example, peaks 4 and 5. The envelope of the peak 4 hides the vibrational states of the symmetry b_1 and a_2 . For the peak 5, the contributions stem from the vibrational modes a_1 and a_2 . Close to the band origin, such ‘blending’ of assignments is rare. Near the absorption maximum, it becomes a rule and an obstacle to an unequivocal assignment.

The mapping approach is reliable for the 15D case. The peak intensities are somewhat underestimated only for the pyrrolyl states involving excitations of the a_1 modes. The intensities of the states with one quantum excitations on non-totally symmetric modes are essentially exact. Not described in the mapping approach are the very weak structures appearing at $\text{TKER} \approx 6000 \text{ cm}^{-1}$. They are populated non-adiabatically, involve an extra quantum of the mode $Q_{a_1}(1)$, and are discussed for the next photon energy window where they are clearly seen.

The TKER spectrum for $E_{\text{ph}} = 4.50 \text{ eV}$ [Fig. 7(b)] corresponds to the absorption band C. The spectrum is arranged in a pattern familiar from the 11D analysis. The blue comb marks peaks already seen at lower energies. These state can be adiabatically connected to the FC excitations of the disappearing modes. The energy spacing between bands A and C is merely 0.15 eV, so it can hardly be related to the excitation of the NH stretch. Instead, an additional excitations of the disappearing bending modes (with the frequencies of 620 cm^{-1} and 1020 cm^{-1}) are adequate candidates. The peaks arising from the excitation

of those states in the band C in the FC zone which have the lowest possible excitation in the disappearing modes are marked red (cf. Table III). New in the 15D case is that the states originating from additional excitations in the \mathbf{R} space (such as peak 5 in the MCTDH calculations or peak 6 in the mapping calculations) have the largest intensities in the TKER spectrum. From the point of view of the mapping approach, which is a faithful representation of the excitation pattern in the FC zone, this indicates that, for example, the state $n_{b_2}(3) = 1$ augmented with an excitation of the disappearing modes, contributes substantially to the assignment of the band C, along with the other ring states indicated in Table III. In the exact quantum dynamics, the peak intensities are further affected by the vibrationally non-adiabatic effects. Indeed, the quantum mechanical intensities of the states under the red comb are consistently lower than predicted in the mapping calculation, while the peaks under the blue comb have higher intensities than in the mapping. The primary reason for this appears to be the nature of the ‘red’ states which, according to Table III, are all combination excitations involving the totally symmetric a_1 excitations. The influence of non-adiabatic interaction during photodissociation tends to depopulate them at the expense of pure ‘blue’ states which have fewer coupling partners at their disposal. This is also seen in the adiabatic curves in Fig. 1(b): In the FC zone the local frequencies of the modes $Q_{a_1}(1)$ and $Q_{a_1}(2)$ oscillate and experience avoided crossings.

The TKER spectrum for $E_{\text{ph}} = 4.65$ eV [Fig. 7(c)] corresponds to the absorption band D and is shown here to illustrate the complexity of the TKER spectra which is achieved with the ab initio Hamiltonian at large photon energies. The number of populated states greatly increases, and a detailed assignment, although technically possible, becomes meaningless without a clear necessity. Nevertheless, the mapping approach remains fairly accurate in this case too, and delivers a correct overall intensity distribution of the TKER peaks.

B. Ab initio quantum mechanics versus experiment

In this Section, the theoretical TKER spectra for the 15D Hamiltonian are compared against the experimental TKER distributions measured by Cronin et al. at long photolysis wavelengths $\lambda \sim 250$ nm using the Rydberg tagging technique.³ The experimental resolution in this wavelength range is high enough to resolve populations of the individual vibrational states of pyrrolyl. As the absorption spectra of the state $1^1A_2(\pi\pi^*)$ has not been measured,

the experimental TKER spectra become the key spectroscopic observables against which the theoretical models can be validated.

Pyrrole is described using the same 15 internal coordinates of the previous Section depicted in Fig. 2. In order to provide a realistic representation of the ab initio TDMs, the functions of Eq. (6) with the R -dependent Herzberg-Teller coefficients are used. The corresponding absorption spectrum is shown in Fig. 3(d). Its overall shape is very similar to the absorption spectrum in Fig. 3(c), calculated for the same set of coordinates but with the R -independent TDM functions. The intensity in panel (d) slightly decreases, the spectrum is broadened by about 10%, while the diffuse vibrational bands are less pronounced. However, the absorption envelope is rather stable with respect to changes in the TDM functions because the photodissociation is fast and the spectral broadening is substantial. More pronounced changes are expected for the TKER distributions. Indeed, the high degree of vibrational adiabaticity, demonstrated in the previous sections, implies that the TDM functions in the FC zone can significantly influence the product state distributions.

Figure 9 compares the calculated and the measured TKER spectra. All results refer to the low energy tail of the absorption spectrum highlighted in Fig. 3(d). The polarization averaged distributions $I_{\text{TKER}}(E_{\text{kin}}|E_{\text{ph}})$ for the rotationless pyrrole are best compared with the TKER profiles measured at the magic angle $\alpha = 54.7^\circ$ between the electric field polarization vector and the detection axis (corresponding to the spectra integrated over α). These data are published for the two longest wavelengths.³ For two shorter wavelengths, the available TKER distributions used in Fig. 9 are for $\alpha = 90^\circ$.

As explained in paper I, the CASPT2 calculations underestimate the vertical excitation energy. In order to make a realistic contact with the experiment of Cronin et al., the calculated TKERs are compared with the experimental distributions associated with the same maximum available kinetic energy $E_{\text{kin}}^{\text{max}}$, i.e. with the kinetic energy of the vibrationless pyrrolyl, $E_{\text{kin}}^{\text{max}} = E_{\text{ph}} - D_0$. The corresponding experimental photolysis wavelengths λ are indicated in the frames (e—h).

The calculated TKER spectra in panels (a—d) are depicted with green lines. All polarizations are included, and — as in the previous section — the TKER spectra peak at vibrational states belonging to all four irreps of the point group C_{2v} . The calculated and the measured distributions are similar in many respects. For example, the significantly populated states for all wavelengths span a narrow kinetic energy window of $\approx 2000 \text{ cm}^{-1}$. Next,

the rotational widths of individual peaks is approximately 50 cm^{-1} implying a cold rotational distribution of pyrrolyl. Figure 4 demonstrates that the rotational excitation of the radical generated upon dissociation of pyrrole- d_5 is stronger than for the case of pyrrole- h_5 .²⁷ Finally, three groups of peaks can be clearly recognized in the TKER spectra, especially at large wavelengths. With decreasing λ , additional peaks become visible in the measured spectra, but the original three groups are still visible.

In principle, the green curves in Fig. 9(a–d) are already sufficient for a line-by-line comparison with experiment and the assignment of the vibrational peaks. However, the inspection of the TKER profiles for each polarization separately, as is done for example in Fig. 8, suggests that the populations of the pyrrolyl states of b_1 symmetry are underestimated in the calculation. In order to facilitate the comparison with experiment, we artificially increase the intensity of the b_1 vibrational peaks by a factor three. This adjustment gives the TKER spectra shown with black lines in panels (a–d). The possible origins of the low population of the b_1 vibrational states in the calculation are discussed in the next section.

The structural similarity between the experimental and the calculated TKERs permits a dynamics based assignment of the experimental spectra. The assignment is easier to summarize for the shortest wavelength shown in Fig. 9(d). In the calculation, this TKER spectrum is very close to the absorption band A and is similar to the TKER spectrum in Fig. 7(a). The R -dependent TDM functions introduce two major modifications into the TKER of Fig. 9(d) as compared to Fig. 7(a): The intensity of the peak corresponding to the ground vibrational state of pyrrolyl is decreased, while the intensity of the peaks around $E_{\text{kin}} = 6000 \text{ cm}^{-1}$ is noticeably enhanced. However, the populated vibrational states are the same, the corresponding peaks are marked with the same numbers in both figures, and their assignments are summarized Table III. The same labeling is also used in Fig. 9(a–c), and the evolution of the TKER spectra with increasing wavelength λ can be easily followed. The experimental peaks in Fig. 9(e–f), for which the correlation with the calculated counterpart is straightforward, are also given the same labels.

The peak 1 corresponds to the ground vibrational state of pyrrolyl and is seen for all excitation wavelengths. In the quantum mechanical TKER, its intensity is gradually decreasing as the wavelength shortens and $E_{\text{kin}}^{\text{max}}$ grows. This is due to the ‘radial factor’ $\bar{\sigma}_R(E_{\text{ph}} - E_0)$ which decreases with growing photon energy. In experiment, the intensity of the peak 1 drops more rapidly than in the calculation which might indicate that the true molecular

potential along the NH bond stretch is steeper than in the calculation, leading to a narrower spectrum $\bar{\sigma}_R(E_{\text{ph}} - E_0)$.

The tiny peak 2, corresponding in the calculation to a one quantum excitation of the out-of-plane ring mode $Q_{a_2}(1)$, can be suspected in the experimental spectrum at 250 nm [panel (f)] and is most conspicuous at 246 nm [panel (h)]. The experimental assignment of this peak to the mode $Q_{b_1}(1)$ (referred to as ν_{21} in Ref. 3) is not confirmed in the calculations: Although the mode $Q_{b_1}(1)$ is included, its population is suppressed by the low value of the Herzberg-Teller coefficient in the TDM function.

The strong peak 3 is attributed to the fundamental excitation of the mode $Q_{b_1}(2)$ ($\omega = 757 \text{ cm}^{-1}$). This coincides with the experimental assignment (this mode is referred to as ν_{20} in Ref. 3). In the calculation, the one quantum excitation of the mode $Q_{b_2}(1)$ ($\omega = 710 \text{ cm}^{-1}$) also makes a minor contribution to the intensity of the peak 3.

The peak 4 is revealed in the calculation only in the vicinity of the absorption band A [panels (c) and (d)]. It is assigned to the fundamental excitation of the mode $Q_{b_1}(3)$, and is found in the experimental TKER as a shoulder of the peak 3 at lower kinetic energies for $\lambda = 248 \text{ nm}$ and 246 nm .

The stronger peak 5 is clearly seen in all calculated and measured TKERs. Its assignment, $n_{a_2}(3) = 1$, agrees with the experimental one (this mode is referred to as ν_9 in Ref. 3), but the relative intensity in the quantum mechanical TKER is overestimated. Note, however, that the population of the $Q_{a_2}(3)$ mode in the experiment is shown to be strongly dependent on the detection angle α : It is large for $\alpha = 0^\circ$ (not shown) and small for $\alpha = 90^\circ$. It is suggested that the vibrational states of a_2 symmetry are associated with large anisotropy parameters.³

Finally, the third group of peaks, labeled 12 — 14, is also reproduced in the calculation. We assign these peaks to the combination states built out of excitations assigned to peaks 3 — 5 augmented with an additional quantum of excitation of the totally symmetric mode $Q_{a_1}(1)$. No specific assignment was proposed on the experimental side, but the authors of Ref. 3 noted that combinations ‘involving one quantum of any of the lower frequency modes of a_1 symmetry’ are possible candidates. Our calculation confirms this suggestion.

V. CONCLUSIONS

This paper analyzes the photofragment kinetic energy distributions of pyrrolyl + H-atom formed in the photodissociation of pyrrole in the low-lying ${}^1A_2(\pi\sigma^*)$ state. The TKER spectra contain complementary and, in fact more precise, information on the fragmentation process than the broad diffuse absorption spectra. The TKER distributions are calculated quantum mechanically using the 1new quasi-diabatic potential energy matrix with elements quadratic in the normal modes of the pyrrolyl ring as described in paper I. It has been demonstrated that the quantum mechanical TKER spectra can also be efficiently and accurately reproduced using the approximate adiabatic mapping approach. Finally, calculated TKER spectra are compared with the experimental results. The main results of our study are summarized as follows:

1. The peaks in the calculated TKER spectra correspond to the few lowest vibrational levels of the pyrrolyl fragment. Sparse TKER distributions are seen in all calculations with 6—15 internal coordinates. States of different symmetries are populated for different electric field polarizations. Photodissociation in the ab initio PES of the state 1A_2 is characterized by a high degree of vibrational adiabaticity, and the TKER profiles are controlled by the initial wave packet shaped by the coordinate dependent transition dipole moment. As a result, the most populated states are the ground vibrational level, the fundamental excitations of the modes mediating the ${}^1A_2 \leftarrow \tilde{X}$ transition, and the states with one quantum excitations along the strongly displaced a_1 modes.
2. The overlap integral-based adiabatic mapping approximation is introduced which generalizes the familiar bound-bound FC spectrum calculations to the case of molecular photodissociation. The mapping approximation accurately reproduces the exact TKER distributions and their dependence on the excitation energy. This method, which requires only a modest numerical effort largely independent of the molecular size, is a promising tool for the analysis of the photodissociation dynamics in large classes of model biochromophores in which sparse TKER spectra are observed.
3. The calculated TKER spectra are in good agreement with the distributions measured in Ref. 3 at wavelengths $\lambda > 246$ nm. The observed populations are reproduced using

the TDM functions which explicitly depend on the NH stretching mode and go beyond the Herzberg-Teller expansion. The correlation between theory and experiment is sufficiently accurate to allow definitive assignment of the measured TKER spectra near the absorption origin.

4. This work proposes a state specific view on the photodissociation of pyrrole and shows its power in explaining the dissociation mechanism. It also demonstrates that combining two approximate methods, the convolution approach to the absorption spectra¹ and the adiabatic mapping of the photofragment distributions, a reliable state specific description can be achieved without the construction of high dimensional potential energy surfaces. A prerequisite for this is a substantial degree of vibrational adiabaticity of the decomposition which is usually well aligned with the state specificity.

The constructed ab initio Hamiltonian for the state ${}^1A_2(\pi\sigma^*)$ allows one to reproduce the experimental TKER spectra around 250 nm fairly accurately. Nevertheless, the agreement between theory and experiment is not perfect. Two sources of the remaining discrepancy can be indicated:

The accuracy of the quantum chemical calculations. The product state populations are strongly dependent on the ring mode frequencies and the potential energy profile along the NH stretching mode R . The frequencies of the ring modes, discussed in paper I, are accurate to within 5% or better for the ground electronic state and the known frequencies of the excited states. However, the vertical excitation energies are systematically underestimated in the CASPT2 calculations. Another source of uncertainty is the quality of the CASSCF TDM function, which affects the intensity and the shape of the partial cross sections proportional to the energy dependent final state populations. The origins of the direct correlation between the TDM function and the observed photofragment distributions are the short time scale of < 50 fs, on which the H-atom dissociates and the vibrational adiabaticity of the reaction. For most vibrational states, the excitation at long wavelengths corresponds to the weak tails of the partial cross section envelopes. For this reason, even small inaccuracies in the PES topography or in the TDM functions can lead to large variations in the TKER spectra. In other words, the photofragment distributions show a typical threshold behavior: A small shift in the relative positions of the partial cross sections of different fragment states produces a large difference in the relative final populations. Pyrrolyl states of all irreps can

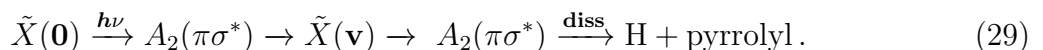
contribute because the TDM components μ_x , μ_y , and μ_z have comparable magnitudes but form different fragments states. One reason for the low population of the b_1 vibrational states in the calculation can be an underestimated R -dependent Herzberg-Teller coefficient for the component μ_y . It is sufficient to increase the magnitude of this coefficient by $\sim 50\%$ to bring the intensity of the b_1 peaks to the observed level.

The functional form of the potential energy surfaces. The constructed potential energy surfaces are quadratic in the ring modes, so that the energy exchange between the vibrations of different symmetries is possible only indirectly via the common coupling to the NH stretching mode R . This affects the vibrational patterns in the TKER spectra and prevents additional fragment states from being directly populated. Moreover, the disappearing angular coordinates are coupled to the pool of the ring modes only via the dissociation coordinate R . This can be another reason for the low populations calculated for the modes of b_1 symmetry. Indeed, the constructed potentials lack coupling between these modes and the out-of-plane H-atom bending and the corresponding bilinear coupling terms are neglected. They could have induced an energy exchange between the ring and the disappearing angular coordinates and affect the populations of the b_1 modes. Finally, one has to keep in mind that the molecular Hamiltonian which is used in the calculations is constructed specifically for the dissociation channel $C_4H_4N + H$. Several other decomposition channels were detected even at low photon energies, and the competing dissociation pathways might indirectly affect the relative populations observed in the H-atom detachment channel.^{6,28–30}

We would like to conclude by commenting on the Fano effect which the conical intersection \tilde{X}/A_2 has on the dissociation dynamics in the lowest $\pi\sigma^*$ state.² In the isolated diabatic state $1^1A_2(\pi\sigma^*)$, pyrrolyl is formed via a direct dissociation path closely following, as explained in Sect. IV, the planar minimum energy path along the coordinate R . Upon adding the coupled ground electronic state and the associated CI \tilde{X}/A_2 to the picture, the radical $C_4H_4N(^2A_2)$ can be formed not only via the direct dissociation of pyrrole,



but also indirectly, with pyrrole making a virtual hop at the intersection, first to an isoenergetic bound state $|\tilde{X}(\mathbf{v})\rangle$ and then back to the continuum of A_2



The interference between these two diabatic reaction pathways is the origin of the Fano effect in the photodissociation.² In the two state absorption spectrum, this interference results in a series of weak asymmetric Fano peaks (‘ripples’) on top of the absorption envelope as illustrated in Fig. 10(b). The resonance structures are enhanced by subtracting the absorption spectrum corresponding to the same parent molecular wave function evolving in the isolated state $1^1A_2(\pi\sigma^*)$. This difference spectrum, also shown in Fig. 10(b), clearly reveals the contribution of the optically dark bound vibrational states of the state \tilde{X} to the total absorption spectrum. The resonance lines in the difference spectrum are grouped into multiplets. The consecutive lines with the highest intensity are found for example near 4.34 eV, 4.47 eV, and 4.58 eV; they are marked with arrows in Fig. 10(b). The spacing between them, of the order of 0.12 eV, matches the frequency of the strongly displaced ring mode $Q_{a1}(1)$. The weaker lines making up the multiplets most probably stem from the anharmonic excitations of the NH stretch which are strong enough to allow a non-negligible amplitude near the CI.

The same interference effect also affects the distributions of pyrrolyl over the product vibrational states. An example is provided in Fig. 10(a) for the photon energy dependent PHOFEX cross section for producing pyrrolyl in the vibrational state with a single excitation of the mode $Q_{a1}(1)$. As in the case of the total absorption spectrum, the Fano interference is best revealed in the difference spectrum taken between the one- and the two state calculation. The resonance structures (also marked with arrows) are correlating well with the multiplets in the absorption spectrum. The vibrational structure of the dark bound states in \tilde{X} is carried over to the asymptotic region and imprinted in the pyrrolyl distributions. At the same time, Fig. 10(a) demonstrates that the Fano peaks in our calculations are most likely not fully converged. Many Fano peaks, clearly seen in panel (b), remain unresolved in panel (a). The reason is the slow population transfer from the state \tilde{X} back to A_2 : Approximately 4% of the population still resides in \tilde{X} even after the 1.2 ps long time evolution. Full convergence of Fano resonances requires much longer propagation times at which high-dimensional MCTDH calculations can become unreliable.

The Fano resonances in Fig. 10 are largely buried in the single state background because the ab initio diabatic coupling between the states \tilde{X} and A_2 is weak. The interstate diabatic coupling is much larger at another CI involving the pair \tilde{X}/B_1 , and for this CI strong Fano interference effects are predicted.² This topic will be discussed in paper III.

Appendix A: Calculation of photofragment distributions with the Heidelberg MCTDH package

The projection method of Balint-Kurti^{16,17} is not implemented within the Heidelberg MCTDH package. The calculation of the photofragment distributions is therefore performed in two steps. In the first step, the time-dependent wavefunction $\Phi(t) = \exp(-i\hat{H}t - \lambda t)\Phi(0)$ is calculated using the MCTDH method and stored at each time step. Once the time propagation terminates, the T -matrix elements are calculated in the second step as follows:

- For each pyrrolyl eigenstate $|\chi_n(\mathbf{Q})\rangle$, the projector $\hat{\mathcal{P}}_n$ of Eq. (19) is constructed in the same MCTDH form which is used in the wave packet calculation. As the Hamiltonian is set in the normal modes of pyrrolyl, it becomes separable as $R \rightarrow \infty$ and the eigenstates $|\chi_n(\mathbf{Q})\rangle$ are obtained as single configurations.
- The time dependent projections of the wave packet on each channel state (the cross correlation functions) are calculated as

$$S_n(t) = \langle \hat{\mathcal{P}}_n^* | \Phi(t) \rangle . \quad (\text{A1})$$

This is the time dependent counterpart of the matrix element $\langle \hat{\mathcal{P}}_n^* | \Psi^\lambda(E_{\text{ph}}) \rangle$ which enters Eq. (20).

- The photon energy-dependent T -matrix elements are obtained as half-Fourier transforms of the cross-correlation functions,

$$T_n(E_{\text{ph}}) \sim \sqrt{\frac{k_n}{m_R}} \int_0^\infty S_n(t) e^{iE_{\text{ph}}t} dt . \quad (\text{A2})$$

Acknowledgments

S.Yu.G. acknowledges the financial support by the Deutsche Forschungsgemeinschaft.

-
- ¹ D. Picconi and S. Yu. Grebenschchikov, preceding paper .
- ² S. Yu. Grebenschchikov and D. Picconi, *Phys. Chem. Chem. Phys.* **19**, 14902 (2017).
- ³ B. Cronin, M. G. D. Nix, R. H. Qadiri and M. N. R. Ashfold, *Phys. Chem. Chem. Phys.* **6**, 5031 (2004).
- ⁴ B. Cronin, A. L. Devine, M. G. D. Nix and M. N. R. Ashfold, *Phys. Chem. Chem. Phys.* **8**, 3440 (2006).
- ⁵ M. N. R. Ashfold, G. A. King, D. Murdock, M. G. D. Nix, T. A. A. Oliver and A. G. Sage, *Phys. Chem. Chem. Phys.* **12**, 1218 (2010).
- ⁶ H. Lippert, H.-H. Ritze, L. V. Hertel and W. Radloff, *Chem. Phys. Chem.* **5**, 1423 (2004).
- ⁷ G. M. Roberts, C. A. Williams, H. Yu, A. S. Chatterley, J. D. Young, S. Ullrich and V. G. Stavros, *Faraday Discuss.* **163**, 95 (2013).
- ⁸ G. Wu, S. P. Neville, O. Schalk, T. Sekikawa, M. N. R. Ashfold, G. A. Worth and A. Stolow, *J. Chem. Phys.* **142**, 074302 (2015).
- ⁹ M. N. R. Ashfold, B. Cronin, A. L. Devine, R. N. Dixon and M. G. D. Nix, *Science* **312**, 1637 (2006).
- ¹⁰ V. Vallet, Z. Lan, S. Mahapatra, A. L. Sobolewski and W. Domcke, *J. Chem. Phys.* **123**, 144307 (2005).
- ¹¹ D. V. Makhov, K. Saita, T. J. Martinez and D. V. Shalashilin, *Phys. Chem. Chem. Phys.* **17**, 3316–3325 (2015).
- ¹² M. H. Beck, A. Jäckle, G. A. Worth and H.-D. Meyer, *Phys. Rep.* **324**, 1 (2000).
- ¹³ H. Köppel, W. Domcke and L. S. Cederbaum, *Adv. Chem. Phys.* **57**, 59 (1984).
- ¹⁴ P. R. Bunker and P. Jensen. *Molecular Symmetry and Spectroscopy*. NRC Research Press, Ottawa, (2006).
- ¹⁵ D. Picconi and S. Yu. Grebenschchikov, *Phys. Chem. Chem. Phys.* **17**, 28931 (2015).
- ¹⁶ G. G. Balint-Kurti, R. N. Dixon and C. C. Marston, *J. Chem. Soc. Faraday Trans.* **86**, 1741 (1990).
- ¹⁷ G. G. Balint-Kurti, *Adv. Chem. Phys.* **128**, 249 (2004).
- ¹⁸ D. E. Manolopoulos and M. H. Alexander, *J. Chem. Phys.* **97**, 2527 (1992).
- ¹⁹ M. H. Alexander, C. Rist and D. E. Manolopoulos, *J. Chem. Phys.* **97**, 4836 (1992).

- ²⁰ The rotational motion of free pyrrolyl treated as a rigid rotor is described using the symmetry adapted combinations of Wigner D -functions D_{k0}^j . Each channel carries, in addition to \mathbf{n} , indices j and k corresponding to pyrrolyl angular momentum and its body-fixed projection; the summation over all channels extends over j and k , too, and the definition of the channel momentum includes the total rotational energy of the radical.
- ²¹ A.M. Perelomov and Ya. B. Zel'dovich. *Quantum Mechanics. Selected Topics*. World Scientific, Singapore, (1998).
- ²² The notation $\varphi_{\mathbf{m}(\mathbf{n})}$ would probably reflect better the adiabatic mapping $\varphi_{\mathbf{m}} \rightarrow \chi_{\mathbf{n}}$, but is awkward to use.
- ²³ M. S. Child and M. Shapiro, *Mol. Phys.* **48**, 111 (1983).
- ²⁴ G. G. Balint-Kurti, *J. Chem. Phys.* **84**, 4443 (1986).
- ²⁵ D. Häusler, P. Andresen and R. Schinke, *J. Chem. Phys.* **87**, 3949 (1987).
- ²⁶ A set of additional symmetry combinations of the final states is in principle thinkable in the photodissociation of pyrrole. These include $(\Gamma_Q = a_2, \Gamma_{\text{ang}} = b_1)$ and $(\Gamma_Q = b_1, \Gamma_{\text{ang}} = a_2)$ for the x -polarized transitions; $(\Gamma_Q = a_2, \Gamma_{\text{ang}} = b_2)$ and $(\Gamma_Q = b_2, \Gamma_{\text{ang}} = a_2)$ for the y -polarized transitions; and $(\Gamma_Q = a_1, \Gamma_{\text{ang}} = a_2)$ for the z polarization. These symmetry combinations of the product wave functions cannot be populated in a single state dissociation, but they become allowed because of the presence of the conical intersection between the states A_2 and \tilde{X} . Consider, as an example, a wave packet initially in the state with symmetry $(\Gamma_Q = a_1, \Gamma_{\text{ang}} = b_2)$ located on the V^{A_2} surface, which first undergoes a transition to the ground electronic state \tilde{X}^1A_1 induced by an a_2 coupling mode, and next makes a second transfer back to the state 1^1A_2 induced by the angular term $\sim \sin^2\theta \sin(2\phi)$. As a result, the final state have the symmetry $(\Gamma_Q = a_2, \Gamma_{\text{ang}} = b_1)$. Although such states are in principle allowed, they are not observed in our simulations, probably due to the weak diabatic coupling along the angular coordinates.
- ²⁷ The distributions in Fig. 4 are for the 3D potential of disappearing modes only, and the average rotational energy of the deuterated radical is enhanced by about 20% which is smaller than the experimental increase of a factor of two reported in Ref. 4.
- ²⁸ D. A. Blank, S. W. North and Y. T. Lee, *Chem. Phys.* **187**, 35 (1994).
- ²⁹ J. Wei, J. Riedel, A. Kuczmann, F. Renth and F. Temps, *J. Chem. Soc. Faraday Disc.* **127**, 267 (2004).
- ³⁰ M. Barbatti, J. Pittner, M. Pederzoli, U. Werner, R. Mitríc, V. Bonacíc-Koutecký, and H. Lis-

chka, Chem. Phys. **375**, 26 (2010).

TABLE I: Expansion coefficients of the TDM function of Eqs. (6). Values are in atomic units [ea_0].

	$\mu^{(0)}(R_{\text{FC}})$	$\mu^{(1)}(R_{\text{FC}})$	$\mu^{(2)}(R_{\text{FC}})$
$\mu_{x,\theta,1}^{A_2}$	-2.04298	-12.2036	-9.33618
$\mu_{x,\theta,2}^{A_2}$	1.19530	6.10336	4.35229
$\mu_{x,1}^{A_2}$	-0.0216261	-0.0216261	-0.0739594
$\mu_{x,3}^{A_2}$	0.030926	0.0297996	0.0018997
$\mu_{x,5}^{A_2}$	0.0166159	-0.0345444	-0.0357879
$\mu_{y,\theta,1}^{A_2}$	3.05435	9.32314	19.0464
$\mu_{y,\theta,2}^{A_2}$	-1.70042	-4.37171	-9.27847
$\mu_{y,1}^{A_2}$	0.00133072	0.0186773	-0.00116267
$\mu_{y,2}^{A_2}$	-0.0261693	-0.0105274	-0.00296679
$\mu_{y,3}^{A_2}$	-0.0219039	0.0505846	0.0469725
$\mu_{z,1}^{A_2}$	-0.022233	0.0534878	0.0889894
$\mu_{z,2}^{A_2}$	0.0246797	-0.111224	-0.154991
$\mu_{z,3}^{A_2}$	0.0340891	0.0166484	0.0265491

TABLE II: Assignments of the TKER spectra in Fig. 6 in terms of the vibrational states of the pyrrolyl ring in the 11D calculations. The absorption bands dominated by the same ring excitations and the obligatory excitations of the disappearing modes ($n_R = 0$) are indicated in the third column. **0** stands for the ground vibrational state of the ring.

TKER peak	Assignment	Absorption band
1	0	A
2	$n_{a1}(1) = 1$	
3	$n_{a1}(2) = 1$	B
4	$n_{a1}(3) = 1$	B
5	$n_{a1}(4) = 1$	
6	$n_{a1}(5) = 1$	C,D
7	$n_{a1}(6) = 1$	
8	$(n_{a1}(1) = 1, n_{a1}(2) = 1)$	
9	$(n_{a1}(1) = 1, n_{a1}(3) = 1)$	
10	$n_{a1}(2) = 2$	D
11	$(n_{a1}(2) = 1, n_{a1}(3) = 1)$	D
12	$(n_{a1}(2) = 1, n_{a1}(4) = 1)$	
13	$(n_{a1}(1) = 1, n_{a1}(5) = 1)$	
14	$(n_{a1}(2) = 1, n_{a1}(5) = 1)$	E
15	$(n_{a1}(3) = 1, n_{a1}(5) = 1)$	E
16	$(n_{a1}(4) = 1, n_{a1}(5) = 1)$	
17	$(n_{a1}(1) = 1, n_{a1}(2) = 2)$	F
18	$(n_{a1}(2) = 2, n_{a1}(3) = 1)$	F

TABLE III: Assignments of the TKER spectra in Fig. 7 in terms of the vibrational states of the pyrrolyl ring in the 15D calculations. Contributions of the excitations via the TDM components μ_x , μ_y , and μ_z are shown separately except for the states of a_1 symmetry which originate from both μ_x and μ_y components. The absorption bands for the y -polarized transition, dominated by the same ring excitations and ' $n_R = 0$ ', are indicated in the fifth column.

TKER peak	Assignment			Absorption band
	μ_x	μ_y	μ_z	
1		0		A
2			$n_{a2}(2) = 1$	
3		$n_{b1}(2) = 1$		A
4		$n_{b1}(3) = 1$	$n_{a2}(2) = 1$	A
5		$n_{a1}(1) = 1$	$n_{a2}(3) = 1$	A,B
6	$n_{b2}(3) = 1$			
7	$n_{b2}(5) = 1$			
8		$n_{a1}(5) = 1$		C
9			$(n_{a1}(2) = 1, n_{a2}(1) = 1)$	C
10		$(n_{a1}(1) = 1, n_{b1}(2) = 1)$		
11		$(n_{a1}(1) = 1, n_{b1}(3) = 1)$	$(n_{a1}(1) = 1, n_{a2}(2) = 1)$	
12		$(n_{a1}(2) = 1, n_{b1}(2) = 1)$		C
13		$(n_{a1}(2) = 1, n_{b1}(3) = 1)$	$(n_{a1}(2) = 1, n_{a2}(2) = 1)$	C
14			$(n_{a1}(2) = 1, n_{a2}(3) = 1)$	C

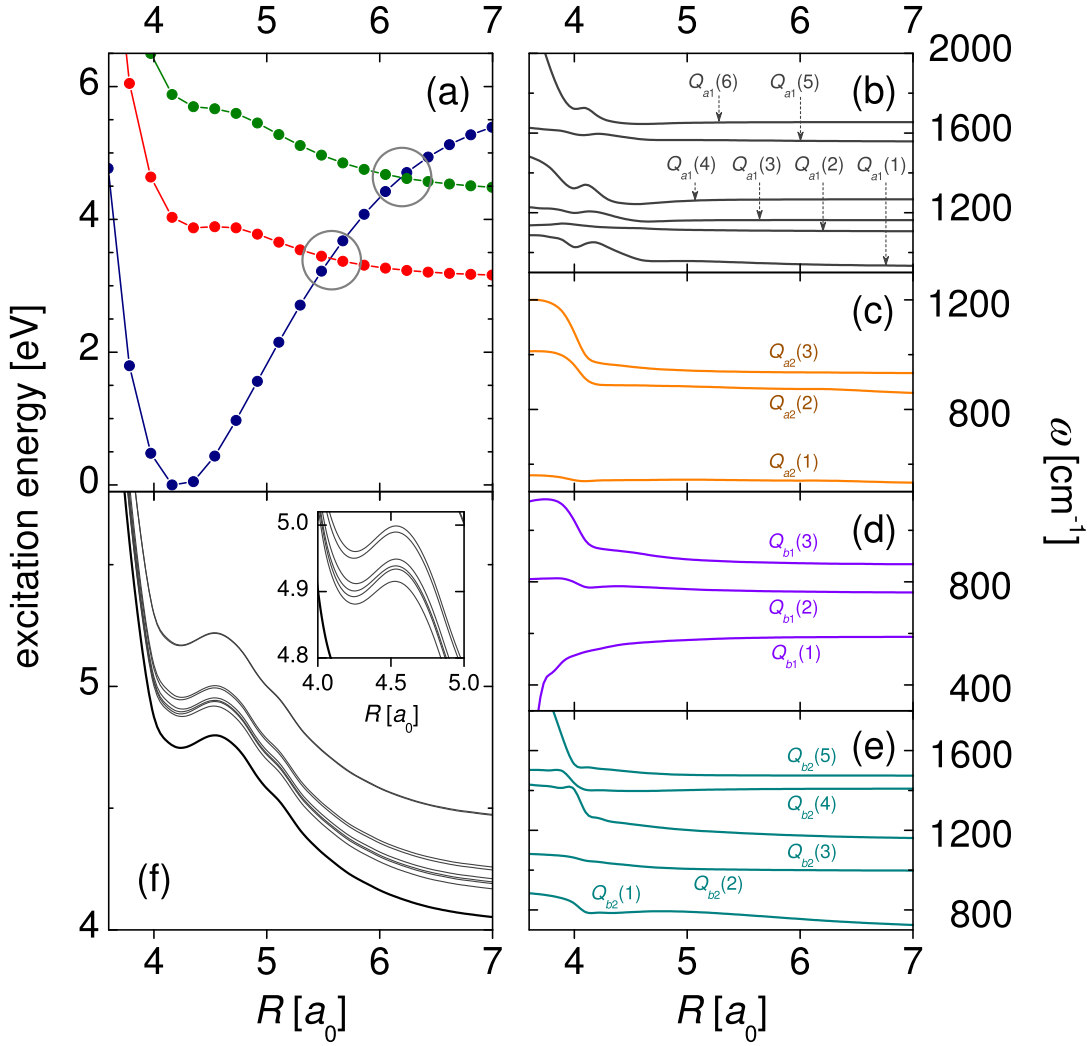


FIG. 1: (a) One-dimensional potential energy cuts of the \tilde{X} (blue), 1A_2 (red), 1B_1 (green) electronic states as functions of the pyrrolyl-H Jacobi distance R . Circles mark the conical intersections. (b—e) Frequencies of the normal modes of the ring of a_1 , a_2 , b_1 , and b_2 symmetry. as functions of R (f) Adiabatic curves $E_m(R)$ constructed as described in Sect. IIIB. The thick black line is the zero-point level, the gray lines represent the states with one quantum on the modes $Q_{a_1}(1, \dots, 8)$.

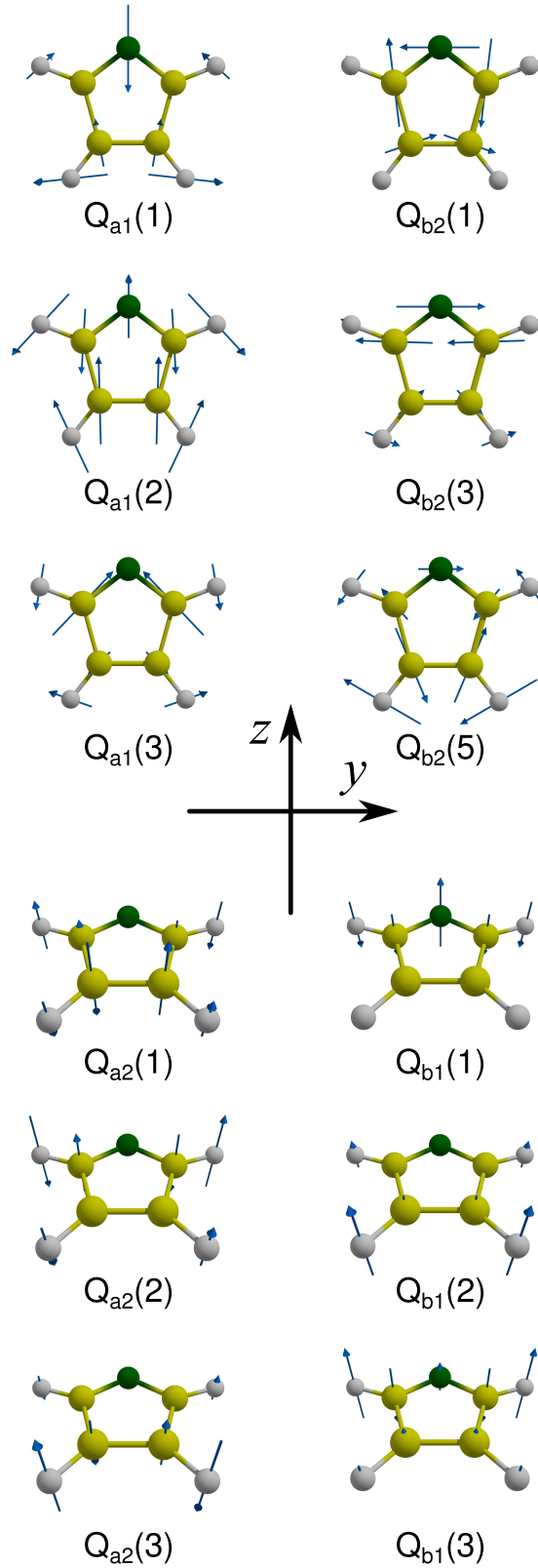


FIG. 2: Sketches of the pyrrolyl normal modes belonging to all four irreps of the C_{2v} symmetry group. These modes are included in the 15D calculations described in Sect. IV A 3. Also shown is the pyrrole axis system in which the components $\mu_{x,y,z}^{A_2}$ of the TDM vector are set. The x axis is perpendicular to the plane of the ring.

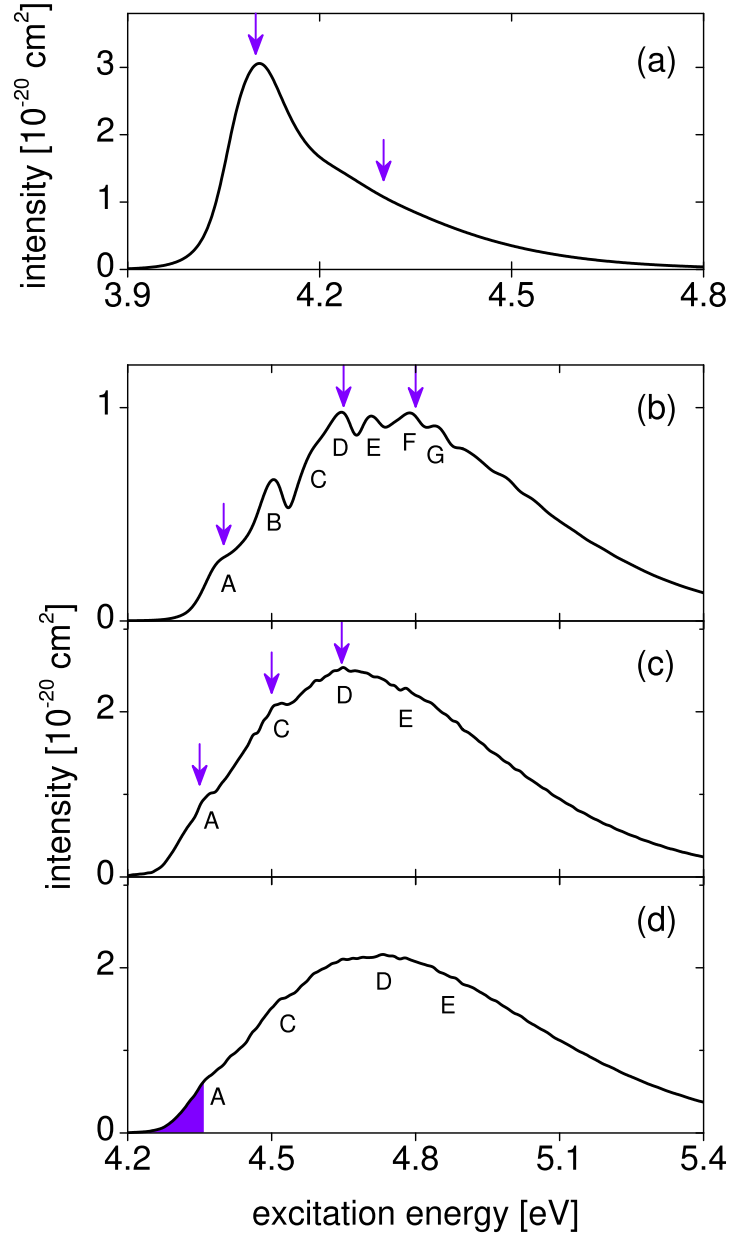


FIG. 3: Absorption spectra for the calculations described in Sect. IV: (a) 6D; (b) 11D; (c,d) 15D. In (a—c), the energies, at which the TKER distributions are analyzed, are marked with arrows. Assignments of the diffuse bands A—F are discussed in paper I. In (d), the TDM functions of Eq. (6) are used, and the area, in which the comparison with the experiment is made, is shaded.

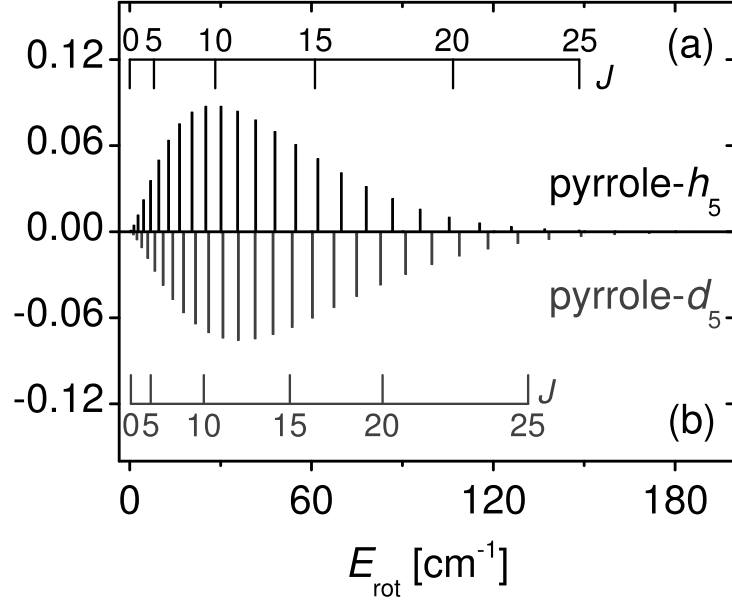


FIG. 4: Rotational distributions of the pyrrolyl fragment formed upon the detachment of the H-atom (a) and D-atom (b) in the state 1^1A_2 described with the 3D potential of the disappearing modes. The TDM function is $\mu_y \sim \sin \theta \cos \phi$. The distributions are shown versus the angular momentum j and the rotational energy E_{rot} of pyrrolyl. The photon energy is equal to the absorption maximum of the spectral function $\bar{\sigma}_R$ (≈ 4.1 eV).

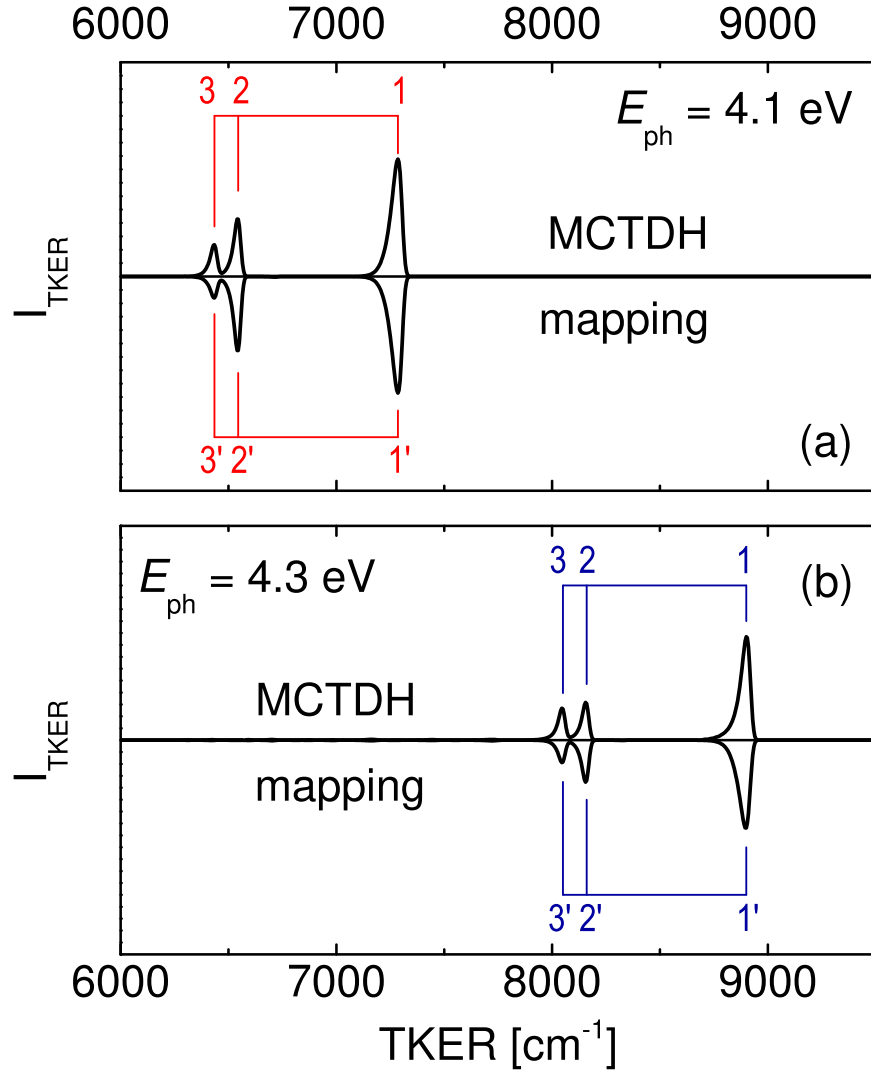


FIG. 5: TKER distributions calculated for the 6D spectrum shown in Fig. 3(a) for the excitation energies (a) $E_{\text{ph}} = 4.1 \text{ eV}$ and (b) $E_{\text{ph}} = 4.3 \text{ eV}$. The quantum mechanical MCTDH distribution is shown in the upper, and the distribution calculated via the adiabatic mapping in the lower half of each panel. The assignments of the peaks marked with combs: *1*. The ground vibrational state $\mathbf{0}$; *2*. $n_{b1}(2) = 1$; *3*. $n_{b1}(3) = 1$. The peaks indicated with red combs stem from the vibrational states in the FC zone carrying the same ring excitation and $n_R = 0$. The peaks indicated with the blue comb correspond to the vibrational states with $n_R = 1$.

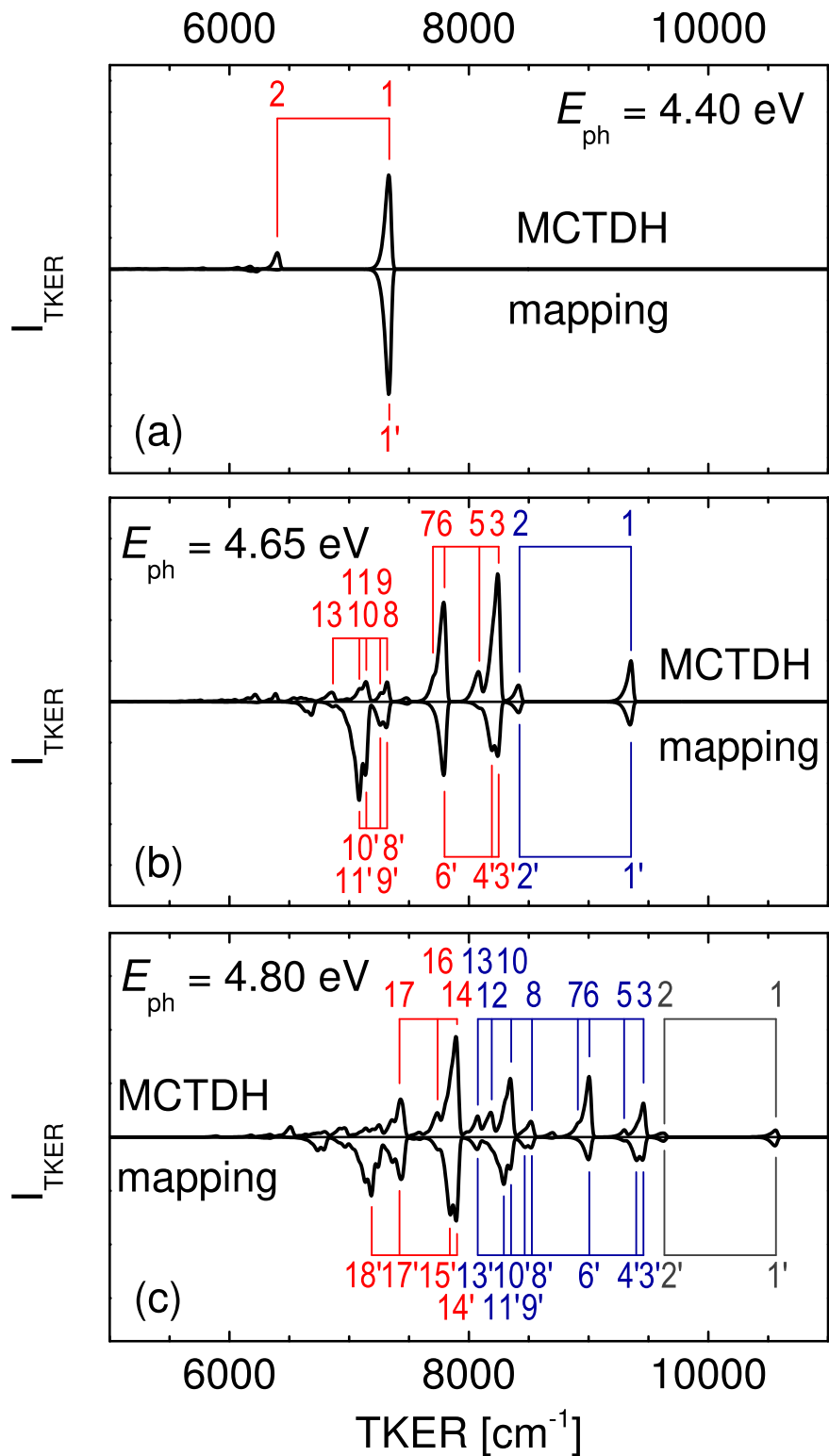


FIG. 6: The polarization averaged TKER spectra calculated for the 11D spectrum of Fig. 3(b) at the excitation energies $E_{\text{ph}} = 4.4 \text{ eV}$ (a), $E_{\text{ph}} = 4.6 \text{ eV}$ (b), and $E_{\text{ph}} = 4.8 \text{ eV}$ (c). The layout follows that of Fig. 5. The assignment combs are colored according to the extent of excitation of the disappearing modes in the FC zone: For the fragment peaks originating from the pyrrole states with $n_R = 0$ and $n_R = 1$, the combs are red and blue; for those stemming from strongly excited

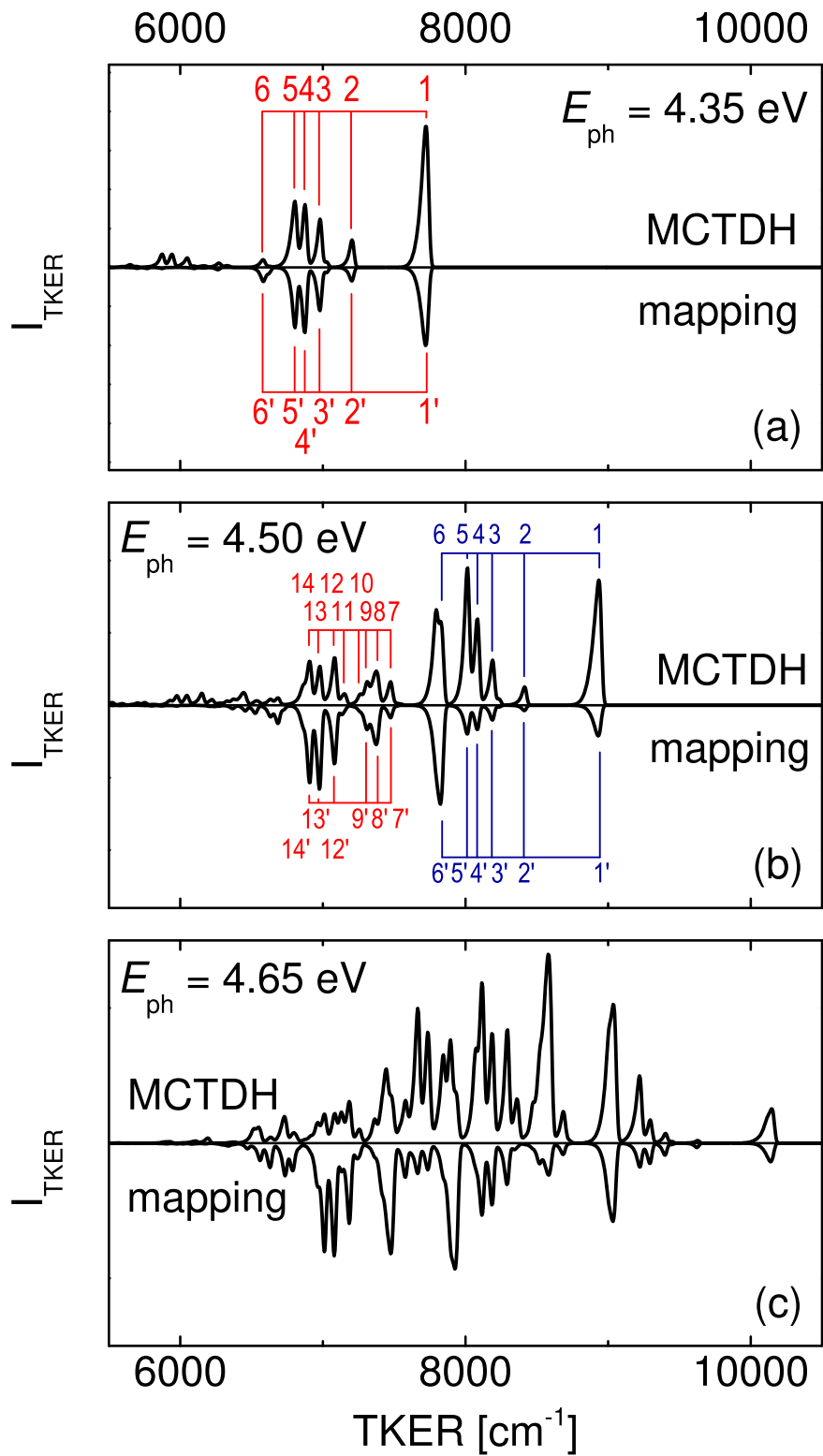


FIG. 7: The polarization averaged TKER distributions calculated for the 15D spectra of Fig. 3(c) at the excitation energies $E_{ph} = 4.35$ eV (a), $E_{ph} = 4.50$ eV (b), and $E_{ph} = 4.65$ eV (c). The layout is the same as in Fig. 6. The assignments are listed in Table III.

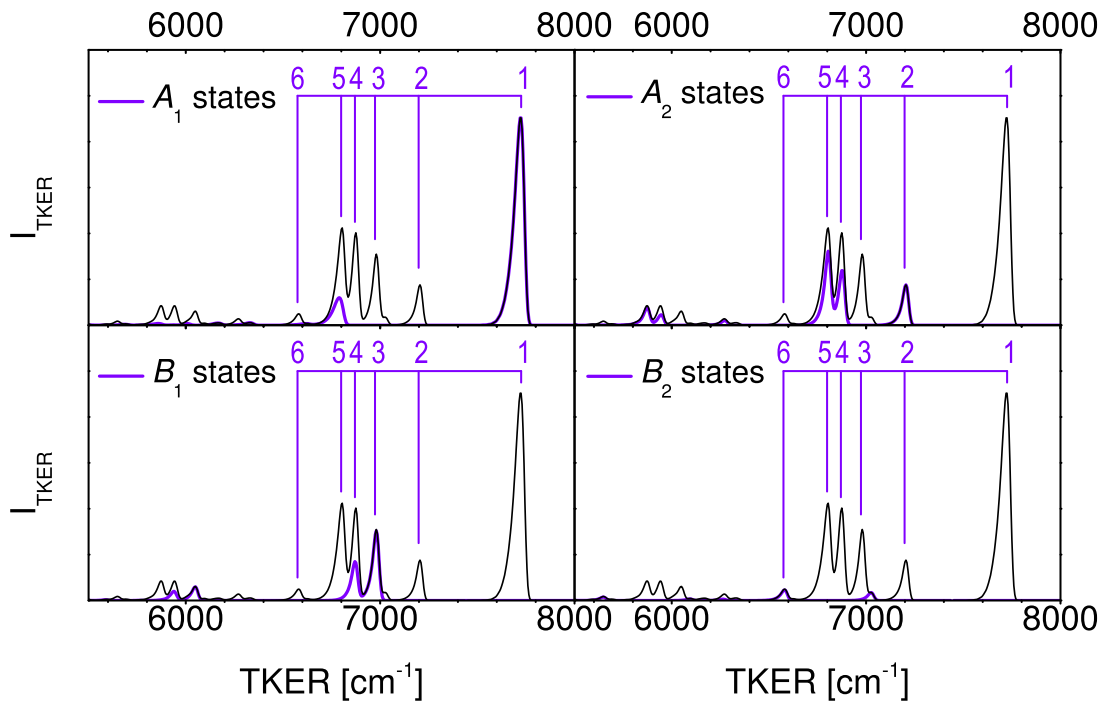


FIG. 8: The quantum mechanical TKER distribution calculated for the 15D spectrum of Fig. 3(c) for $E_{\text{ph}} = 4.35$ eV (thin gray line), decomposed into the contributions corresponding to the four symmetry blocks of the C_{2v} point group (thick purple lines).

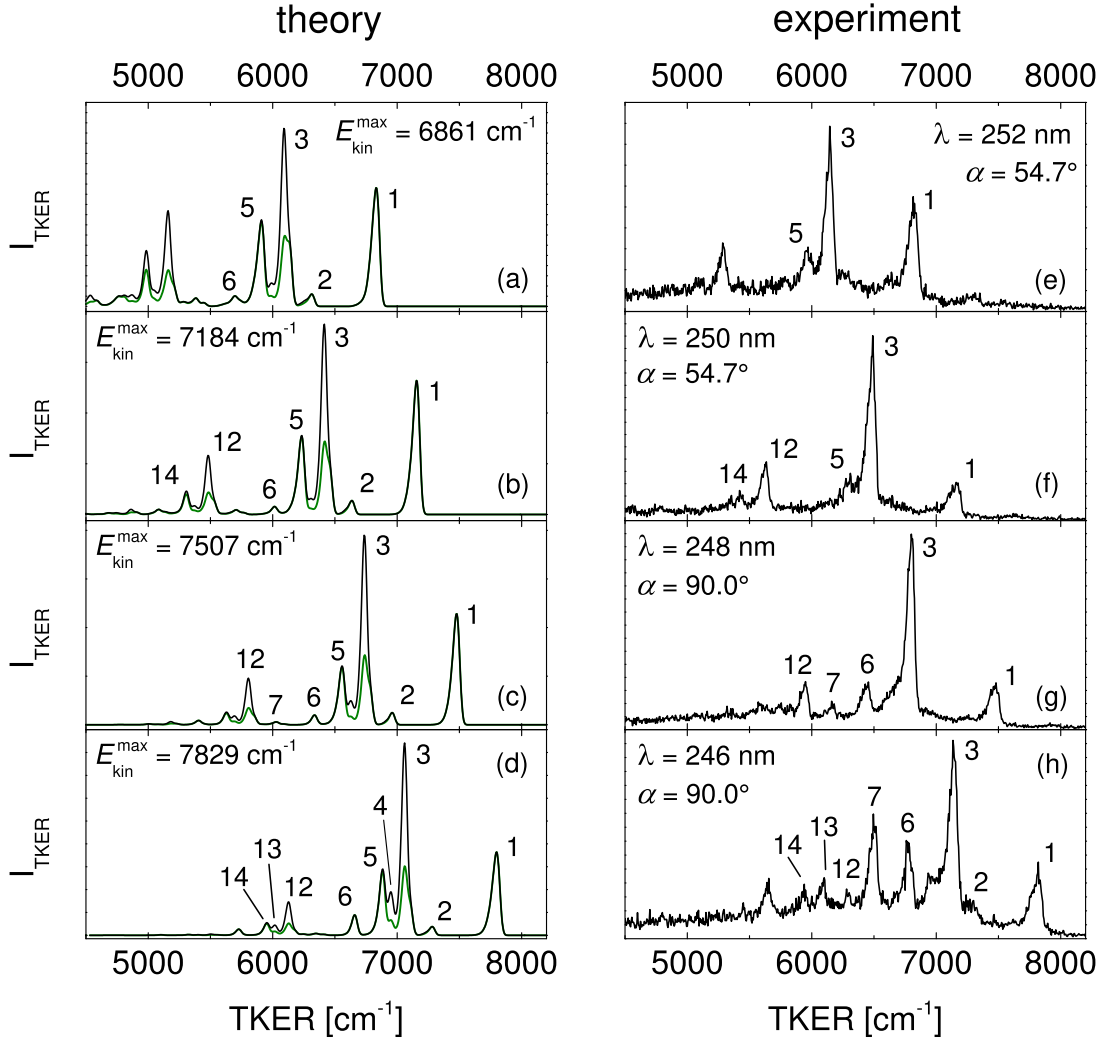


FIG. 9: (a-d) The 15D polarization-averaged TKER spectra calculated with the R -dependent TDM functions (green dashed line). The profiles shown with the solid black line are obtained by increasing the population of the pyrrolyl vibrational states of b_1 symmetry by a factor three. The kinetic energy $E_{\text{kin}}^{\text{max}}$ of the peak corresponding to vibrationless pyrrolyl is indicated in each panel. (e-h) Experimental TKER spectra of Ref. 3 with similar $E_{\text{kin}}^{\text{max}}$ as in the respective panels on the left. The detection angle α and the experimental excitation wavelengths are indicated in each panel. The assignments are listed in Table III.

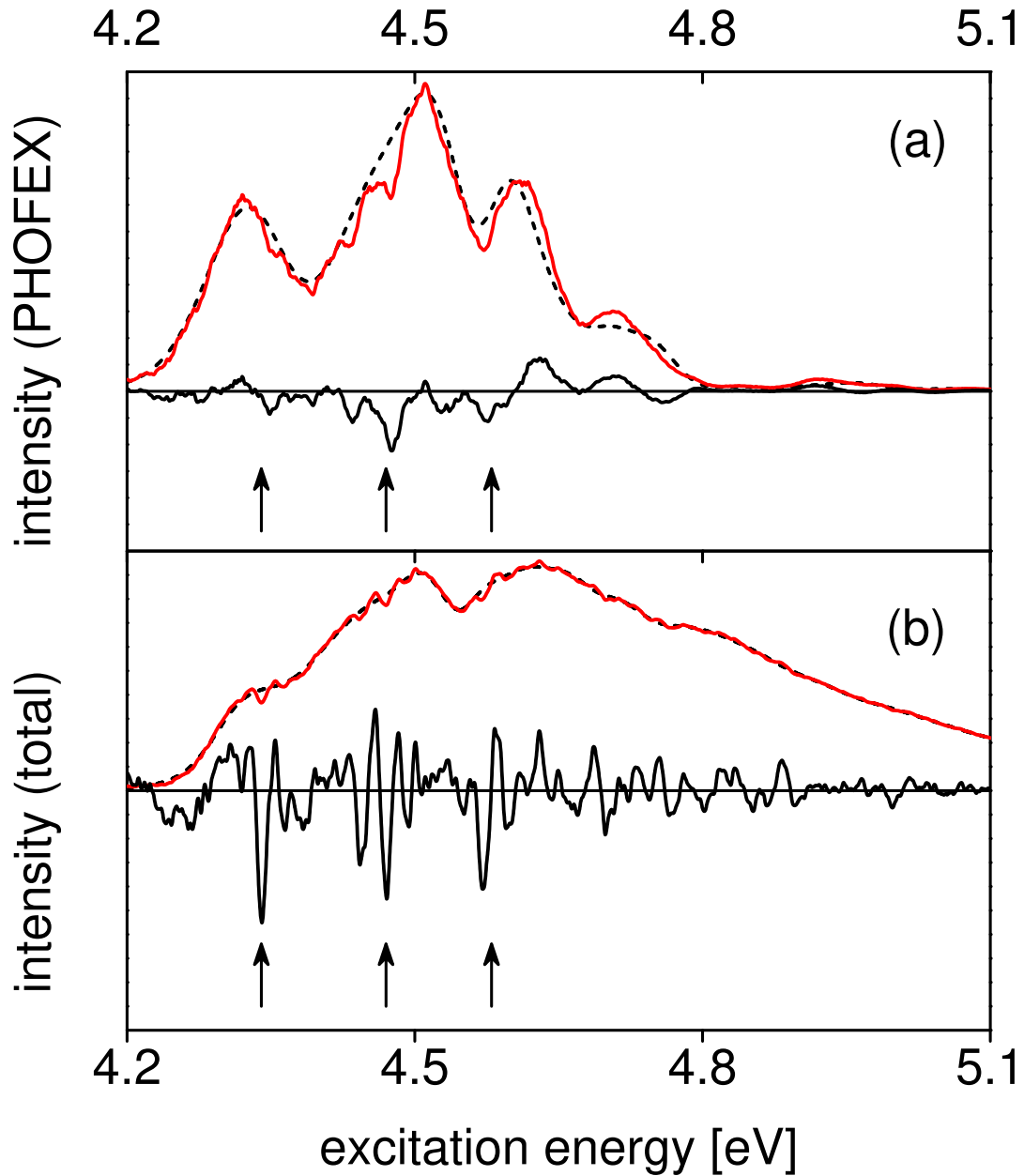


FIG. 10: (a) The partial cross section (the PHOFEX spectrum) for the formation of pyrrolyl in the vibrational state with one quantum of the mode $Q_{a_1}(1)$ as a function of the photon energy. The dashed black curve is calculated for the single state 1^1A_2 ; the solid red curve is for the pair \tilde{X}/A_2 . The solid black line is the difference spectrum. (b) The total absorption spectrum calculated using the TDM $\mu_y \sim \sin \theta \cos \phi$. The dashed black curve is calculated for the single state 1^1A_2 ; the solid blue curve is for the pair \tilde{X}/A_2 . The solid black line is the difference spectrum, multiplied by a factor 10. Arrows in both panels mark the highest intensity lines in the consecutive multiplets of Fano resonances. All calculations are for the 15D case.